Design and Optimization of Carbon-Fiber Chassis Panels

Eric C. Anderson

Thesis submitted to the Faculty of the Virginia Polytechnic Institute and State University in partial fulfillment of the requirements for the degree of

Master of Science
in
Mechanical Engineering

Robert L. West, Chair
John M. Kennedy
Scott W. Case

May 27, 2014
Blacksburg, Virginia

Keywords: Finite Element, Composite, Optimization, Formula SAE, Chassis

Design and Optimization of Carbon-Fiber Chassis Panels
Eric C. Anderson

Abstract

Each year, the Virginia Tech (VT) Formula SAE (FSAE) team creates a high performance car to compete against 120 teams from around the world in a series of dynamic events evaluating acceleration, maneuverability, and handling. In an effort to improve upon the VT 2013 car, the torsional stiffness of the chassis was increased. Increasing the torsional stiffness of the chassis allows the suspension to be more precisely tuned, resulting in a better overall performance. An investigation was conducted into methods for improving the chassis stiffness, and it was determined that many state-of-the-art vehicles from go-karts to super cars incorporate strength-bearing, tailored advanced composite materials in their structure. Examples of components that use composites in vehicles include sandwich structures in load-bearing panels, layups in the skin of vehicles for aesthetic purposes and carbon-fiber frame tubes. The VT FSAE car already includes untailored carbon-fiber panels on the bottom and sides of the structure for packaging and aerodynamic purposes. By integrating and optimizing these carbon-fiber panels, the torsional stiffness and therefore overall performance of the structure may be increased.

This thesis explores composite testing, optimization methods, experimental and computational analysis of the chassis, and results. The fiber orientation of the panels may be optimized because carbon-fiber composite materials are generally anisotropic. Therefore the composite materials can be tailored to maximize the stiffness, resulting in the optimum stiffness per added weight. A good measure for testing stiffness per added weight is through measuring natural frequencies because natural frequency is proportional to stiffness per unit mass. A computer program was developed in MATLAB to optimize the composite configuration, and uses an objective function involving the first three natural frequencies of the original steel space frame chassis and the first three natural frequencies of the steel chassis augmented with three composite panels. The composite material properties were determined using specimen tensile testing and checked with finite elements. The natural frequencies of the half-scale chassis were determined experimentally, compared to the simulated version, and varied by less than seven percent. The optimization of the full-scale model determined that eight layers of optimized, integrated carbon-fiber composite panels will increase the first, second, and third natural frequencies by sixteen, twenty-six, and six percent, respectively. Natural frequency increases of these amounts show that by using tailored, load-bearing composite panels in the structure, the torsional stiffness of the structure increases, resulting in easier suspension tuning and better performance at the VT FSAE competitions.

Acknowledgments

I would like to express special appreciation and thanks to my committee chair and advisor, Dr. Robert West, who has guided my research into this field. I would also like to express my gratitude to my committee members, Dr. John Kennedy and Dr. Scott Case, for their helpful advice and support. I would like to thank Composite Fabrics of America for donating 75 yards of 3k carbon fiber to the VT FSAE team this year, which was used in this research. I would also like to thank the VT FSAE team for helping to build the composite specimens.

Contents

List of Figures

List of Tables

Nomenclature

Ply Coordinate System	Coordinate System of the Individual Ply
Local coordinate System	Coordinate System of the Total Laminate
1-Direction	Fiber Direction
2-Direction	Direction Perpendicular to the Fiber in the Plane
3-Direction	Out of Plane Direction
Compliance Matrix	S-Matrix Multiplied by Local Stresses to Calculate Local Strains
Stiffness Matrix	C-Matrix Multiplied by Local Strains to Calculate Local Stresses
Transformation Matrix	Multiplied by Global Strains to Calculate Local Strains
$\bar{Q}$ Matrix	Multiplied by the Global Strains to Calculate Global Stresses
ABD Matrix	Matrix Showing Properties of Laminate Configurations
ϵ	Axial Strain
σ	Axial Stress
γ	Shear Strain
τ	Shear Stress
N	Force Resultant
M	Moment Resultant
ϵ^0	Reference Surface Strain
κ^0	Reference Surface Curvature
δ	Extensometer Displacement at ith Data Point (in)
L_g	Extensometer Gage Length (in)
P	Force at ith Data Point (lbf)
A	Average Cross Sectional Area (in^2)
E^{chord}	Tensile Chord Modulus
$\delta\sigma$	Difference Between Applied Stress at Two Different Data Points
$\delta\epsilon$	Difference Between Strain at the Same Two Different Data Points
ν	Poisson's Ratio
ϵ_{lat}	Difference in Lateral Strain Between Two Longitudinal Strain Points
ϵ_{long}	Difference Between Two Longitudinal Strain Points

1 Introduction

1.1 Overview

The Formula SAE (FSAE) Collegiate Design Series is a Society of Automotive Engineers sanctioned event that pits the abilities of the Virginia Tech FSAE team against the teams of 120 universities around the world. The car, built by undergraduate students, participates in several different events. The four dynamic events are acceleration, skid-pad, autocross, and endurance. The acceleration event is conducted as seventy-five meter race to evaluate the straight-line acceleration capabilities of the car. The skidpad event is a figure-eight course designed to measure the lateral acceleration capabilities of each car. The handling and maneuverability of the car is tested in the autocross event over a tight course. Endurance is a twenty-two kilometer race where durability and fuel efficiency are evaluated.

The Virginia Tech 2013 car performed well in the FSAE Michigan competition, but there are still areas for improvement such as frame nodal coordinate positioning, tire modeling, and loading the attached carbon-fiber panels. This work investigates integrating tailored carbon-fiber panels to increase the stiffness in the chassis. Currently, carbon-fiber panels are attached to the bottom and sides of the frame, but are not tailored for optimal stiffness. The current carbon-fiber panels provide aerodynamic and packaging benefits, but their use was simply an added weight to the structure from a stiffness perspective.

1.2 Needs and Hypothesis

The car needs to improve each year to stay competitive with the other entries which are similarly improving their designs. One area that may potentially provide significant improvement is the frame stiffness. The chassis of the car needs to be as light-weight and as rigid as possible so that the team can get the most out of the suspension system. The suspension of the car must be tuned to improve handling of inertia forces during cornering, braking, and acceleration events, resulting in better lap times and a higher overall performance.

A flexible chassis couples with the suspension dynamics, making it difficult to maximize the performance. By increasing the natural frequencies of the chassis, the suspension and the chassis may be improved separately as they are decoupled. Designing and building several super cars from the ground up using advanced composite materials resulted in stiff, light, and effective car bodies and frames [15-20]. If the current steel space frame chassis is augmented with tailored and integrated composite panels with a sandwich structure, then the chassis will be stiffer and perform better on the track. This thesis will use finite element analysis and an optimization code to determine the optimum panel orientation for maximum stiffness per unit mass of the chassis.

1.3 Goals and Scope

This thesis will investigate the potential to increase the stiffness of the original chassis by integrating tailored carbon-fiber panels to the cockpit area of the chassis. In vehicle racing, adding weight to a system, if nothing else changes, is detrimental to the speed. Natural frequency is proportional to stiffness per unit mass, making it a measure of performance for potential solutions. A stiffer chassis, which uses mass in a more effective way, will have a higher natural frequency. A result of a higher first torsional, first lateral bending and first transverse bending frequency is better performance.

A goal of this project will be to increase the natural frequencies of the system by tailoring and integrating carbon-fiber panels. This work will establish computational modeling techniques and compare to an experiment using a half-scale chassis. Following that, composite material properties will be determined. By using experimental and computational modal analysis techniques to determine the natural frequencies of the chassis, the integrated carbon-fiber panels will be optimized to find the stiffest and lightest potential structure. The stiffest structure may potentially include two-eight tailored carbon-fiber plies and a foam core to separate the 8-ply composite laminates of the structure.

1.4 Organization of Thesis

The focus of tasks within the scope of this thesis are composite testing, analysis of the steel structures, and optimizing the carbon-fiber panels. The composite tests are based on the ASTM D3039 Standard

Test Method for Tensile Properties of Polymer Matrix Composite Materials [1]. The analysis of the steel and subsequent numerical modeling will discuss the natural frequencies, the damping ratio and the testing involved. Pre and post-processing programs have been developed and refined to integrate with the Abaqus finite element code [2] to build and optimize the full structure.

A useful source for information on the manufacturing, design and analysis of composites is MIL-HDBK-17-3F [3], a military handbook discussing a wide range of composite information and design guidelines. MIL-HDBK-17-3F [3] describes a conservative method to designing and implementing composites into a structure known as the "Building Block Approach," shown in Figure 1. The purpose of this approach is to work from the most basic composite structure - the individual lamina - to the full-scale tests of a structure. Moving upwards from level to level, the designer/analyst uses supporting technologies and design requirements to ensure that the design stays within acceptable bounds. Throughout the process, the designer/analyst uses computer-aided analysis, where practical, to speed up and supplement the physical tests conducted simultaneously.

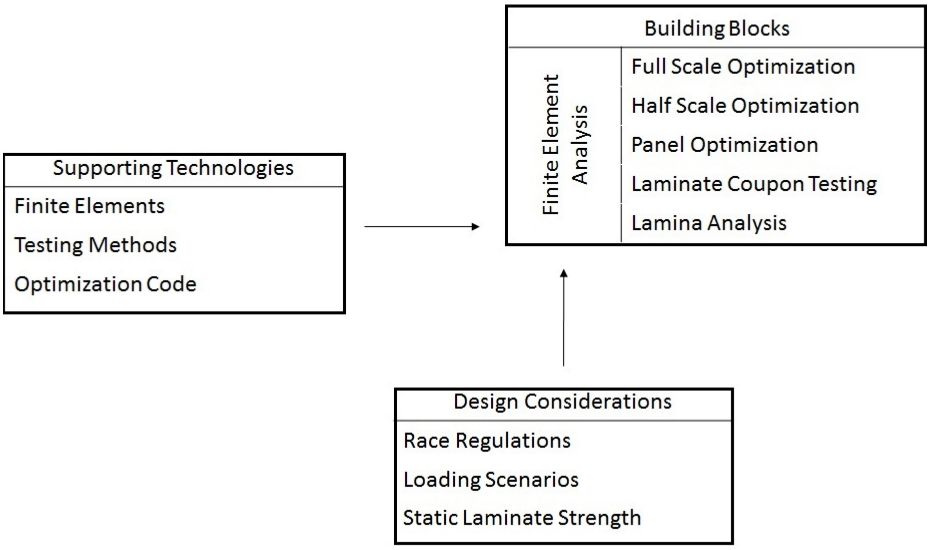

Figure 1: An application of the "Building Block Approach" based on the approach outlined in MIL-HDBK-17-3F Reference 3.

This thesis will discuss the design considerations, such as the forces the chassis will experience during operating conditions, as well as supporting technologies, such as finite elements and optimization approaches to improve the structure. Not all of the potential design variables may be adjusted due to race regulations on several components of the car [4].

Seventy-five yards of 3k carbon fiber [0/90] fabric was donated to the team in 2013 by Composite Fabrics of America, and is the material used to build the laminates. Coupon tests will be conducted on fully constructed eight-layer carbon-fiber reinforced composite laminates. The stacking sequence, not the lamina weave, will be a design variable. The material properties will be developed through coupon testing. Tensile coupon tests on 10" x 1" coupons will be conducted, and simulated with the Abaqus commercial finite element code.

After the laminates have been analyzed, material properties for a full array of ply orientations and laminate stacking sequences will be available through classical lamination theory (CLT). A half-scale chassis model, built for modal test purposes, will be analyzed and compared to a finite element simulation. This will provide confidence in the finite element modeling technique and process. The VT FSAE full-scale chassis model will be optimized computationally, and the optimal stacking sequence will be found. The stacking sequence and this methodology of integrated panel stiffness improvement can be implemented on the 2015 VT FSAE chassis.

2 Literature Review

This section discusses the state-of-the-art research methods and standards for composite material testing, frequency analysis, and the design of advanced composite materials. In addition, it discusses the optimization of carbon fiber components and vehicle chassis.

2.1 Finite Element Analysis

The major computer analysis tools used to optimize the composites in their various configurations will be Abaqus and MATLAB. Abaqus is a commercially available nonlinear finite element code. MATLAB is a high-level language and interactive environment for numerical computation, visualization, and programming. For the optimization procedures, MATLAB will run Abaqus and optimize using a MathWorks Optimization Toolbox minimization function. This thesis describes the objective functions, constraints on the problem, and bounds on the design variables to achieve the results.

The chassis was simulated as shown in Figure 2. The section profiles are either square or circular tubes with specified dimensions. The basic beam element has two nodes with each node given a rotation and a displacement, however, the beam elements used in this program have six degrees of freedom per node. Those six degrees of freedom include translation in any direction and rotation about any axis as shown in Figure 3. The beam has properties of Young's Modulus (E), principal area moment of inertia about the primary bending axis (I_1), principal area moment of inertia about the secondary bending axis (I_2), polar moment of inertia (J), Area (A), and Length (L) [5]. In Abaqus, this type of element in called a B32 element, and is representative of a beam element in 3-D space with three nodes in a quadratic formulation. Each of the potential conventional shell elements have 4-9 elements [5]. The simplest model is a bilinear element with three degrees of freedom (x,y,z translation) at each corner. While this is computationally inexpensive, the elements cannot accurately represent bending in the structure. The element used in Abaqus to model the composite panels is the S8R. It is an eight node model implementing reduced integration.

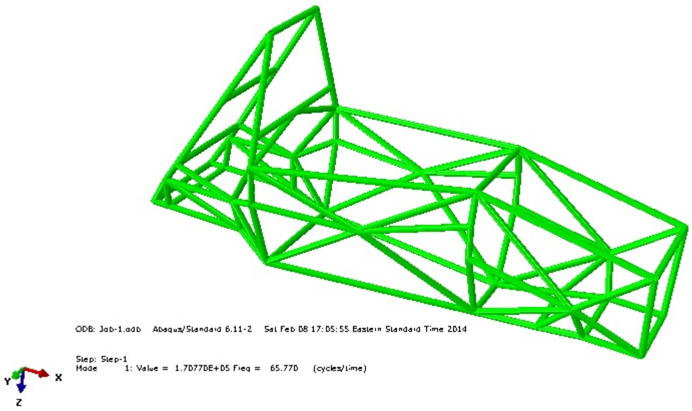

Figure 2: Frame of beam elements of different profiles.

2.2 Design Considerations

The composite used to strengthen the chassis, without adding a significant amount of extra weight, was a hand-laid, bi-axial woven composite. Tensile testing produces the composite material properties used in the analysis of the structure. The ASTM standard for the standard Test Method for Tensile Properties of Polymer Matrix Composite Materials (D3039) [2] discusses the in-plane tensile properties of composite materials and applies to the composites under investigation. The ASTM D3039 Standard [2] determines the maximum strain-to-failure using strain gages in testing. The rate of deformation was controlled with an Instron load frame, and is discussed in the composite analysis section of this thesis. The Young's modulus and Poisson's ratio are calculated.

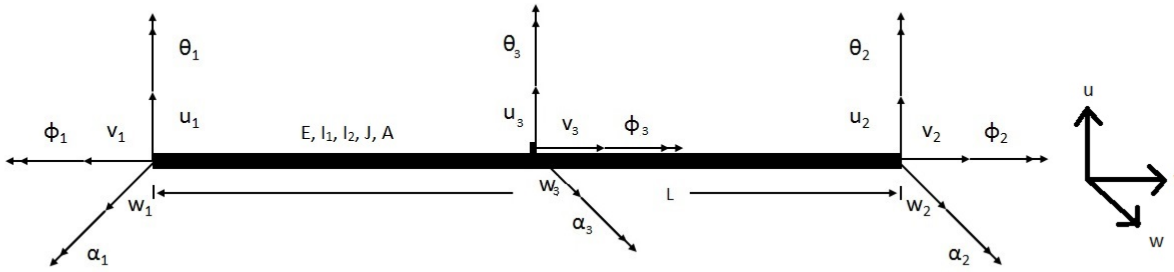

Figure 3: A basic beam element with associated degrees of freedom at every node.

Chen [6] documented an approach on an affordable approach for robust design of thick laminated composite structure. In it, a systematic approach to develop a design for a composite hip implant is proposed. Chen [6] uses a multi-level optimization procedure to improve the compression strength of the hip-joint product. The algorithm uses a response surface methodology to achieve rapid convergence of the problem while maintaining minimal variance of the performance. An effective method for thick sections of composite by classifying the problem with three levels: global (laminate), global (sub-laminate), local (ply) is detailed. These three levels are solved in sequence so as to find the required stiffness at the global, inter-ply and the individual ply levels, and the ply orientations as a result. Chen's [6] procedure can be applied to the design of integrated composite structure in the FSAE car in a slightly different manner, as the chassis system uses thin sheets, not thick sections. The multi-level approach can view the side and bottom panels as separate entities and rather than optimizing all the variables simultaneously, the sections may be optimized individually to save time. If the systematic approach Chen developed is used, a robust solution may be found.

The stiffness of the panels was optimized in order to determine the "best" laminate thickness and stacking sequence. A constrained minimization problem is expressed, as shown in Equations 1 to 3 [7]. The goal is to develop a minimization function that accurately represents the problem and will be discussed in a later section. Because the stacking sequence needs to have orientations between -90 and +90 degrees, the bounds on one of the variables of x will be $-\pi/2$ to $\pi/2$.

$$Minimizef(x) = objectivefunction \tag{1}$$

$$x_{j,lb} < x_j < x_{j,ub}, j = 1, 2, 3..., n \tag{2}$$

subject to:

$$h_k = 0, k = 1, 2, 3, ..., n \tag{3}$$

The approach to optimization of composites involves satisfying strength and weight constraints while using variables such as stacking sequence, ply orientation, thickness, and material. Bruyneel [8] shows that optimizing the fiber orientations can produce effective results while staying within strength constraints. A proposed problem with an initially unsafe laminate is optimized in the paper in one of three way: increase the thickness, optimize the orientation, or both simultaneously. It is proven that a higher stiffness-to-weight ratio can be achieved through the optimization of both ply thickness and orientation at the same time. The Tsai Wu strength criterion is used as a constraint and must be less than one. This thesis will optimize the FSAE car's bottom and side panel's orientation and stacking sequences simultaneously.

Another optimization technique analyzes the effect of bending-twisting coupling on torque tubes under a combination of torque and in-plane loading. A paper authored by Walker [9] uses the Tsai Wu failure criterion as the objective function. The goal is to minimize the failure criteria as theta is varied from zero to ninety. From this value, another optimization sequence optimizes the in-plane loading on the tube. The approach of this work will be to simultaneously optimize the number of plies and the orientation of those plies with the sum of the normalized natural frequencies as the objective function

The work also takes into account that the chassis as a whole will not be made up of just one panel, but rather three panels around the center line of the structure. The panels will interact with each other. To prevent additional coupling in the structure due to their placement around the longitudinal center of the chassis. Karaolis [10] shows what effect the panels may cause. If the two side panels are symmetric, additional bending-twist coupling of the structure will occur. If the side panels are balanced with respect to each other, stretching twisting coupling can occur.

The panels were be bonded to the car in such a way as to activate bending moment capabilities of the laminated panel. A simplified version for analysis represents the panel as simply supported on all sides. Whitney [11] details the analysis of a simply supported plate in bending. By following the analysis, it is determined that the bending of the plate and the maximum deflection associated therewith will be caused by the D matrix entirely and the geometry of the plate, in this case, assumed to be rectangular [11]. In fact, the maximum displacement will be determined by the inverse of the D_{11} element of the D matrix [11]. If the bending-bending elements are reduced, the stiffness of the panel should be increased.

2.3 Component Testing and Analysis

A chassis structure is stressed by both the internal loads, such as mass and inertia, as well as by external loads due to environment and interaction between the wheels and the ground [12]. The chassis has three parts called the frames, underbodies, and sub-frames [12]. The three components combine and form a space frame chassis, where the different longitudinal and cross-frame elements are placed to provide mounts for various components needed for operation. The next step in the frame development process is to advance the space frame to a stressed-skin/monocoque chassis, where the panels on the frame are load bearing and assist in increasing the specific torsional stiffness of the chassis.

The chassis has a few important features and several problems which can be solved by increasing the torsional stiffness. The tread of the chassis is the distance between the center points of the ground contact of wheels on opposite sides of the vehicle [13]. The wheelbase is the distance between the center points of the ground contact of wheels on the same side of the car [13]. Increasing or decreasing these values can greatly affect the handling and maneuverability of the chassis in question. Early cars had an open body structure, resulting in poor torsional stiffness. A weak torsional stiffness is related to door jamming, an ill-fitting hood, and front end shake [13]. These three problems can be fixed in one of several ways, including arranging frame members, or adding cross members so that shocks, which would normally cause torsion in the chassis, will result in bending moments [13]. By increasing the torsional stiffness, the handling of the vehicle will increase as well. There are several open bays in this chassis which can be enclosed with composite panels to increase the stiffness. The composite panels should be tailored to provide optimum torsional stiffness.

2.4 Natural Frequency analysis

A frequency response function displays the resonant frequencies of a system. To develop a frequency response function (frf) from an experiment, a force is applied to a structure and the resulting displacement at any chosen point is measured. To generate the frf over a range of frequencies, the frequency of the forcing function must vary across the span of frequencies [14]. Peaks occur at locations where the resulting displacement is higher than the surrounding frequencies, and these peaks occur at the dampened natural frequencies of the system. To get the natural frequencies, the conversion from ω_d to ω_n is calculated using Equation 4. For metal structures with very low damping, the value under the square root should be very close to one. For metal structures such as the steel frame of the chassis, the value of ω_d is assumed to equal ω_n when in a free-free configuration without integrated composite panels. Determining the damping ratio of the composite panels is not within the scope of this project.

$$\omega_n = \frac{\omega_d}{\sqrt{1-\zeta^2}} \tag{4}$$

where:
ω_n = Natural frequency (Hz)
ω_d = Damped natural frequency (Hz)
ζ = Damping ratio

2.5 Structural Optimization of Chassis

This section of the literature review discusses several studies which have designed and optimized a composite laminate stacking sequence on automobiles. The automobiles vary from low performance to high performance, but all have been improved from the tailored use of composites. To tailor the composites means to build the laminate in such a way as to improve identified properties of the car. A common way to use carbon fiber is to make what is called "black aluminum." Black aluminum is a common laminate stacking sequence which exhibits the same material properties in all directions in the plane of the laminate. An example stacking sequence for this type of stacking sequence is $[0/+45/-45/90]_S$. Stacking in this way will cause the material properties to be similar to aluminum. However, this is not tailoring composites and does not result in the optimal configuration most of the time. A simple example of tailoring is if a square panel will experience only shear, only put ±45 degree laminates in the layup, as this will make it stronger in the shear direction.

The simplest example of a full vehicle is a go-kart. Biancolini [15] describes the design and optimization of a go-kart as "unconventional" due to the lack of suspension systems in the vehicles. The paper describes in detail the reference structure upon which design improvements will be made. The reference structure is a flat steel frame which has a proposed replacement by a carbon fiber plate with a honeycomb structure in the center. Several different models of balanced, cross ply laminates with varying thicknesses of the honeycomb structure have been simulated. A similar factor of safety can be developed using a carbon fiber sandwich structure [15]. Accelerations are applied to reference structure and three different composite layups and were analyzed. It was found that the carbon fiber structure can experience similar and even greater values for stiffness and smaller deflections than the original steel structure. Using a sandwich structure within the carbon fiber panel will help to increase the total strength of the system and push its stiffness higher than that of the steel structure alone. This improvement will be studied in this thesis.

A zero emission vehicle is another case where, to be as efficient as possible, the weight of the car must be reduced. Cristello [16] wrote a paper on optimizing a ladder frame chassis (not a space frame) of a zero emission vehicle by optimizing the chassis mass, deceleration during collision, and ease of hydroforming [16]. A ladder frame chassis has rails on both sides of the car, and members that connect the rails, but the chassis does not extend far in the vertical direction. Design constraints on the torsional stiffness, bending stiffness, natural frequencies of the first torsion and bending modes, and maximum von-Mises stresses are included in the analyses [16]. The optimization process proceeded in three parts. First, the number and location of cross members was determined. Second, the profiles of the cross members was optimized with mass and strength being design variables. Third, the mass, deceleration in the event of a crash and the hydroformability was considered as the whole structure was developed as a parametric model in ANSYS [16]. It is imperative that the location of the nodes of the chassis be optimized in the future to better fit carbon-fiber panels. To get the best results, one will need to optimize in order: the location of the nodes, the profiles of the tubes, the location of the carbon-fiber panels, and finally the orientation of the carbon fiber panels.

A very high performance class of vehicles is that of land speed record holders. These vehicles must be stiff in bending and stiff in torsion so that vehicle handling is not compromised. The vehicle's space frame structure has been proposed to be changed to either a semi-monocoque or fully-monocoque composite sandwich structure. For these races, the vehicle's inertial resistance is far greater than aerodynamic drag, so if the designer can decrease the mass of the structure without sacrificing stiffness a higher speed will be achieved [17]. The three configurations analyzed by Biancolini [17] include the original space frame, a bottom composite plate, bottom and side composite plates and monocoque structure [17]. To compare each structure, the torsional stiffness is calculated using Equation 5. Several elements such as the motor and hydrogen tanks are modeled as either rigid, solid structures or point mass additions to the structure. The results of the analyses of the stiffness show that the stiffest model is a semi-monocoque structure with steel beam reinforcements in the rear of the structure. The torsional stiffness of the space frame increases only when the bottom section of the space frame is replaced with a carbon-fiber structure and decreases when the side struts are also replaced with composite panels. It may become apparent that replacing a large amount of the steel in the structure with composite materials may impede the improvement of the car.

$$K_t = \frac{M_t}{\theta_t} \tag{5}$$

where:
K_t = Torsional stiffness (lbf in/rad)
M_t = Applied torsional moment (lbf in)
θ_t = Torsional rotation (rad)

Super cars use carbon fibers in a variety of locations. In the case of the Lamborghini Murcielago, Feraboli, Paolo and Masini [18] discuss the development of composite components - carbon fiber in particular. A major advantage of using carbon-fiber technology to replace steel frames is both weight reduction and part consolidation. Feraboli, Paolo and Masini [18]describe using ASTM standard D790 (discussed above) to get inter-laminar shear stresses and other material properties. The authors note that a unidirectional tape oriented in a quasi-isotropic laminate is preferable to a woven fabric because ”they [the tape] do not present a high degree of anisotropy” [18]. The anisotropy referred to is the coupling components of the laminates, which were explained earlier in this work. Their design of the laminate is a 3-ply balanced asymmetric composite that utilizes a honeycomb core and a twill in the most exterior ply to achieve a high surface finish [18]. The surface finish is needed for aesthetic purposes for high-end consumer products. Importantly, the authors mention that because they use a balanced, asymmetric laminate, the mold for the laminates are a complex shape, so that when the panels cool and deform, they deform into the shape that is required for the body panels of the car [18]. For this work, only symmetric laminates will be considered to avoid the complex molds required.

A step up from the complexity of the Lamborghini Murcielago, is the Lamborghini Murcielago roadster. The difference is that the car does not have a permanent roof. A result of this on normal cars is the loss of up to 50% of the torsional rigidity [19]. To combat torsional rigidity loss, the structure has been reinforced throughout the sub-frame and the engine bay compartment with tubular elliptical composite members. The elliptical members were molded with a male-female mold, so that one is on the inside and the other is on the outside. These allow the easier orientation of fiber layups. Masini [19] states that with the addition of several reinforcing members, the car achieved the ”desired value of torsional rigidity”. An addition area to investigate regarding the addition of carbon-fiber in the VT FSAE car chassis is the tubes themselves and whether replacing them will give a better solution.

The Cavazzuti paper [20] couples the optimization of topology, topometry, and size with a finite element analysis of a Ferrari 458 Italia. The objective function (the function used to determine fitness of a configuration) is weight reduction that is constrained by Ferrari strength requirements. For this program, the wheelbase, track, suspension layout, suspension joint positions, and the passenger compartment size and locations are fixed [20]. A spider frame (no roof) structure is the basis. If the strength is not adequate, a roof can be added to increase the strength of the structure. The bending and torsional stiffness are measured by applying moments and measuring deflections. In particular, the torsional stiffness is measured by loading the front right wheel vertically (all others fixed), while the change in θ is the difference in angles between the front wheels and the rear wheels. The structure is developed as a material density problem, where for each iteration, the material density at different locations is reduced in order to determine the most optimum structure [20]. The computation time and resulting solution to using the material density method is not applicable to the scope of this work; however, the stiffness measurements, constraints, and loading scenarios are quite applicable.

2.6 Analyzing the Full-Scale Model

Analyzing the full-scale model could involve dynamic analysis, as it did in Angelini's [21]. He conducted a dynamic analysis on the Virginia Tech 2012 Formula SAE car under several different loading scenarios. The scenarios he chose were the basis of loading situations the car might experience traveling around the track, such as a bump or turn. Through the analysis, he was able to determine several structurally weak locations which could be improved. He concluded that without accurate tire models he would be unable to get accurate loading scenarios to simulate within the finite element model.

Heiβing [22] states that because the interaction of the chassis with the suspension system and wheels is difficult, it is sometimes important to analyze the results of standard driving maneuvers, which agrees with Angelini's [21] conclusions following his work on the matter. The standard driving maneuvers include braking, turning, cornering, and a combination of the three. Several load cases were used to compare the original chassis to a set of optimized frames.

3 Half-Scale Experiment

This section of the thesis will detail the experimental procedure for finding the half-scale chassis' natural frequencies. This half-scale experiment is included because it establishes the modeling techniques and accuracy of modeling the welded joints of a steel structure. The results of the frequency analyses of the half-scale chassis will be shown here; however, the comparison with the computer model will be discussed in the next two sections. The first nine natural frequencies that were found during the experimental testing are tabulated to show that the model and simulations are comparable past the first three natural frequencies.

3.1 Set-up

The attempt is made to have the experimental system be as close to the free-free boundary conditions as possible. This is accomplished by suspending the structure using long (sixty inch) bungee cords, so that the natural frequencies associated with the swaying, twisting and bouncing of the system be as low as possible. The bungee cords will be characterized and the natural frequencies associated with the bungee-cord suspension method will be determined. In this case, Figure 4 shows the relative length of the sixty inch bungee cords. The high length results in low swaying natural frequencies. Experiments were conducted by constraining the top of a bungee cords and attaching varying weights to the end of the bungee. From the weight applied and the resulting elastic extension, Equation 6 is used to determine the linear spring constant. The spring constant of the bungee cords increased in a linear fashion for the weights chosen as shown in Figure 5, where the sloping line shows the experimental results and the flat line shows the average result. While the bungee cord spring constant varied across the weight region, due to the length of the cords, the calculated natural frequencies will not be adversely affected. The weights were chosen such that the weight of the chassis, when dived over the four supporting springs falls within the tested region. The average spring constant for the bungee cord was determined to be .244 lbf/in.

$$F = kx \tag{6}$$

where:
$F =$ Applied force (lbf)
$k =$ Spring constant (lbf/in)
$x =$ Displacement (in)

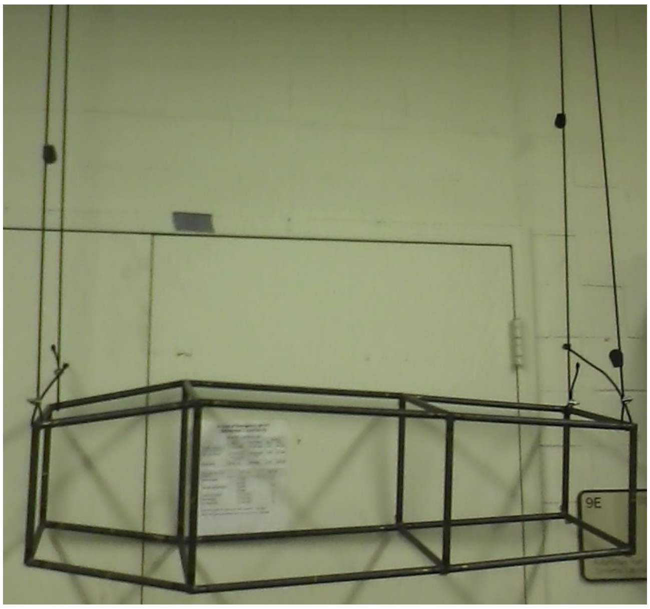

Figure 4: The suspension of the frame is with bungee cords attached to the ceiling.

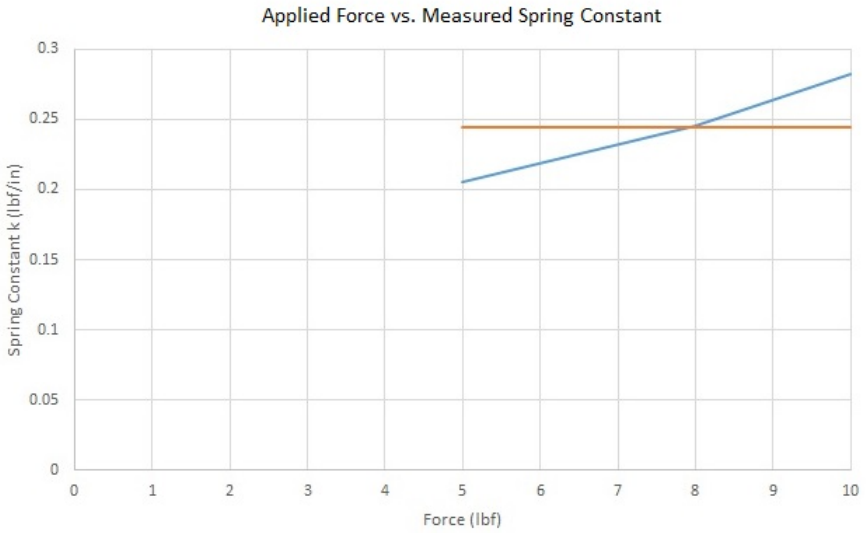

Figure 5: The extension of the bungee cords as a result of different applied masses. The red line is the average which is used in the analysis and the blue line covers the experimentally tested spring constants of the bungee-cords.

An external force is applied to the structure via a shaker with an impedance head measurement. A shaker excites the system over a range of frequencies and an accelerometer records the accelerations at different points in the system. The accelerometer used is PCB model 352C04 with relevant properties listed in Appendix B. The comparison between the two results in a frequency response function, specifying the natural frequencies of the system. The permanent magnet shaker, Ling Dynamics Systems model V203, is suspended to provide force in a given direction and align the force vector with the direction of the mechanical impedence sensor, PCB model 288D01. The relevant frequency and weight properties of the shaker and impedence head are given in Appendix B. The stinger attached to the shaker helps to ensure that force perpendicular to the applied direction does to affect the system. The shaker is also suspended so that any boundary conditions associated with it will not affect the system as shown in Figure 6. The figure shows the shaker's harness and the stinger attached to the shaker which connects the force gage/impedance head to the frame. In this experiment, several pipes run the length of the ceiling and the same pipe used to hold the end of the frame aligns and supports the shaker. The accelerometers which record the acceleration of different points of the system and in specific direction are attached to the chassis by attachment points and accelerometer wax as shown in Figure 7. The accelerometer in the figure sits on an attachment point next to a bungee attachment point of the system, but far enough away to not interfere with data collection. The accelerometer is shifted from point to point between tests in order to retrieve the acceleration data at different locations on the structure.

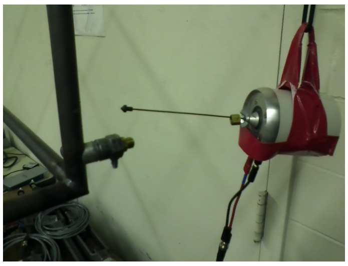

Figure 6: Suspended shaker with stinger attached.

The machine used to gather data is a Hewlett Packard 35665A Digital Signal Analyzer with settings described below. The machine is set to a two-channel frequency response with an upper display and a lower display, where one is the phase and the other is the response of the system in decibels. Both channels are setup so that AC Coupling, Anti-aliasing, and ICP supply are on. The excitation source

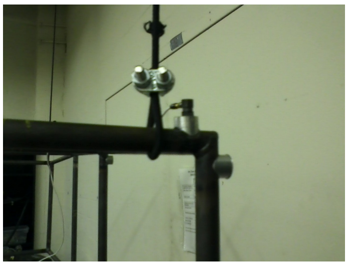

Figure 7: Accelerometer attached to the structure via accelerometer wax.

signal is set to periodic chirp with a 200 mV peak level in order to get a good signal to noise ratio (on the order of .998) in the FFT window. The frequency is tested over 50 Hz ranges from 20-220 (Frequency ranges of 20-70 Hz, 70-120 Hz, 120-170 Hz, 170-220 Hz) so that the coherence and signal to noise ratio can be maximized over the desired set of natural frequencies. The lower limit of the frequency is chosen as 20 Hz because that is the lowest frequency that the system can achieve due to limits on the measurement abilities of the impedance head. The lowest value to get results from the accelerometer and impedance head/force gage is approximately 10 Hz, but the coherence of the signal at those levels were too low to get accurate data. Each result was the compilation of twenty-five averages to further decrease the noise of the system and to increase the accuracy.

3.2 Frequency Analysis Results

The goal of the experimental setup was to design a modal test configuration where the chassis is as close to free-free boundary conditions as possible. This was achieved by suspending the chassis from 60 inch long bungee cords, keeping the modes associated with swaying and twisting low compared to the structural frequencies of the system. Even with the 60 inch long cords, the physical swaying modes of the bungee-cord suspension system should still be measured. To determine this, the chassis was tested in these swaying and twisting modes. An initial displacement was given to the system and the period associated with the motion was timed. It was determined that swaying parallel to the long side of the structure has a frequency of 0.427 Hz, swaying perpendicular to the long side has a frequency of 0.400 Hz and twisting has a frequency of .578 Hz. As the lowest structural natural frequency of the structure (Torsion 1) occurs at 54 Hz, the frequencies associated with the swaying motion are two orders of magnitude smaller and will not interfere with the other modes of the system.

The frequency analysis results in different values based on the position of the accelerometer on the frame. Different values occur as different mode shapes of the system do not excite all points on the system. The positions chosen for this test are shown and labeled in Figure 8 and Appendix A lists the coordinates of the system. The points 1-4 are on the bottom face, facing downwards and the points 5-8 are on the rear face, directed towards the wall shown in the Figure. In this orientation, the chassis is excited at point 6. The chassis was also excited at point 2, after it was rotated ninety degrees so points 1-4 face the wall. Points 2 and 6 were chosen to be the attachment points because of their proximity to the corners of the structure allowing any excitation to potentially trigger the bending and torsional natural frequencies of the system. Corners 2 and 3 rest directly under a pipe from which the chassis is suspended. To this same pipe (along the same line of action) is attached the shaker, resulting in alignment with the VT FSAE chassis frame.

Table 1 shows an example of the results to determine the first six natural frequencies of the system. For this example the frame is situated as shown in Figure 8, and the shaker is attached at position 6 and the accelerometer at position 3. The resonance frequencies and anti-resonance frequencies recovered from the digital signal analyzer are tabulated in Table 1. When viewed in this manner, one can see that most of the peaks of the system are well separated, meaning that each peak has a minimal affect on the neighboring modes.

The eigenvalue frequency testing was conducted at every labeled point on the structure for the orientation shown in Figure 8, and at a ninety degree rotation about the longitudinal axis, resulting in 14

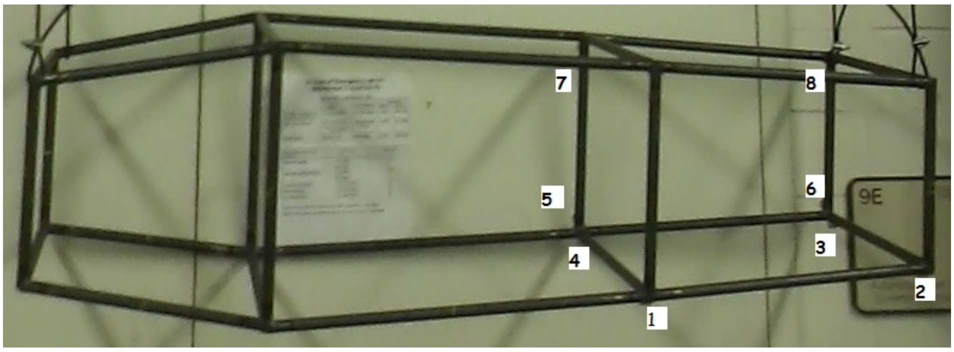

Figure 8: Numbered acceleration attachment points.

Table 1: Example list of experimentally generated frequencies. Node 3 was measured from an excitation by the shaker at node 6.

Excited at	Recovered From	Range (Hz)	freq (Hz)	phase change?	Antimode?	Coherence
6	3	20-120	51	Yes	Yes	0.956
		20-120	82.5	Yes	No	0.990
		20-220	86.75	Yes	No	0.935
		20-220	107	Yes	No	0.994
		20-220	129	Yes	No	0.999
		20-220	154	Yes	No	0.999

data sets. Each set of twenty-five averages resulted in slightly different values for the natural frequencies, as expected. In more than one case, an anomalous natural frequency was determined that few or no other accelerometer locations registered. Stating that, each data set shared several common natural frequencies. Table 2 shows the set of common frequencies present over the whole range of data sets. The frequencies displayed are only those which appear in at least five of the data sets. For the most part, the modes are well separated with two around 80 Hz that are the exception.

Table 2: List of experimentally generated frequencies.

Frequency (Hz)
51
82.5
86.75
93
100
108
122
129
154

4 Half-Scale Finite Element Analysis

This section of the document will discuss the simulation developed to represent the half-scale system. The relevant data input to the program are described and the results from the frequency analysis of the computer system are shown.

4.1 Set-up

The same geometry present in the experimental setup is present in the computer model. The geometry of the model - that is the nodal positions relative to a reference point - are listed in table format in Appendix A. In addition, because the chassis is made out of steel tubes with a radius .3125 inches and thickness .035 inches, these values are also input into the computer model and are listed in Appendix A. Each section of tubing is one element long for the natural frequency approximation and uses a quadratic beam element in space (a B32 element). The convergence of the half-scale simulation is .11 percent of the first natural frequency and is shown in Table 3.

Table 3: Convergence of the first natural frequency of the half-scale chassis.

Number of Elements	Natural frequency (Hz)	% difference
28	54.44	
56	54.38	0.113
84	54.38	0.0047

In addition to the geometry used in the system, the bungee cords will be accurately simulated so that similar structures may be compared. The bungee cords will be modeled as spring elements with the experimentally determined spring constant of .244 lbf/in. The stiffness value calculated from the bungee cord extension tests, shown in Figure 5 in the previous section, is input into the model. In addition, the length of 60 inches is also used as the length of the springs in Abaqus. The top of the springs (at what would be the ceiling) have been set to the boundary condition *Encastre*, restricting all translation and rotation degrees of freedom at the node representing the ceiling. The boundary conditions of the system have thus been established and measured to match closely the boundary conditions in the lab. Figure 9 shows the system as modeled in Abaqus.

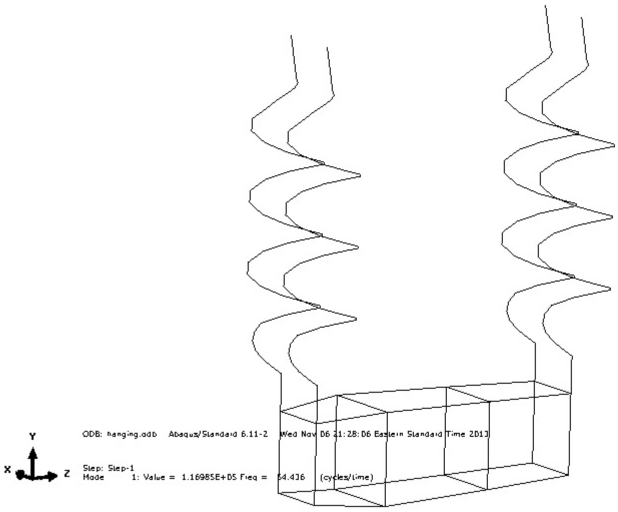

Figure 9: The chassis-bungee system as modeled in Abaqus. The springs have been fully constrained at the top.

4.2 Finite Element Frequency Analysis Results

Abaqus delivers a plot of the amplitude of the mass normalized mode shape when natural frequencies of a system are requested. The computer simulation determined the modes of the system under 170 Hz, as this represented the range of the frequencies tested experimentally. The computer simulation with the geometry described found the natural frequencies listed in Table 4. The simulation determined that the natural frequencies of the system are quite well separated.

Table 4: Natural frequencies calucated with the computer simulation.

Frequency (Hz)
54.4
85.8
91.1
101.4
117.1
132.5

The finite element program outputs the displacement at each node both visually and numerically. These two outputs will help to determine whether the natural frequencies (which are similar between the experiment and simulation) can be the same mode shape. A selection of mode shapes will be displayed below, along with descriptions of the displacements predicted by accelerometers at the points mentioned in Figure 8. The four natural frequencies studied as examples are 54, 86, 117, and 132 Hz. Their mode shapes, shown as an image of the whole frame, as well as what the directional accelerometers should register, will be discussed. The comparison of the simulation to the experiments can be found in the next section of this document.

The mode shapes at frequencies 54, 86, 117, and 132 are shown in Figures 10, 11, 12, and 13. The 82 Hz mode shape did not appear in the Abaqus result. This may be due to the added mass of the shaker being absent from the computational analysis. The 54 Hz frequency is the first torsional mode of the structure. Every point on the structure is in motion in the X-, Y-, and Z- directions with the majority of the motion occurring in the cockpit of the structure. The second and third mode shapes are bending modes of the structure, where the nodes only move in the vertical or transverse directions. This bending mode would not be able to be witnessed by an accelerometer orthogonal to the direction of motion. For the 86 and 117 Hz cases as well, the center section experiences the greatest amount of deformation. The 132 Hz bending mode appears to be a torsional mode of the structure, with every accelerometer witnessing motion of the structure. Interestingly, the front section of the chassis is deformed at 132 Hz leading to the conclusion that after the cockpit is reinforced, the next step is to work on the front section of the vehicle. A comparison between the mode shapes found with Abaqus and experimentally will be conducted in the next section.

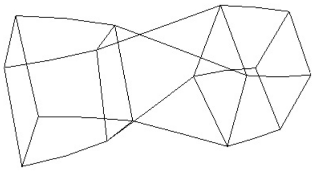

Figure 10: Free-Free half-scale chassis first torsional mode at 54 Hz.

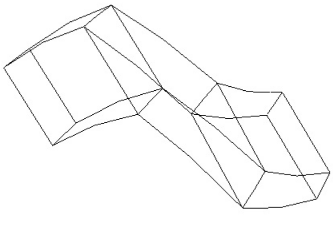

Figure 11: Free-Free half-scale chassis first shearing mode at 86 Hz.

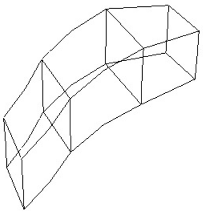

Figure 12: Free-Free half-scale chassis first bending mode at 117 Hz.

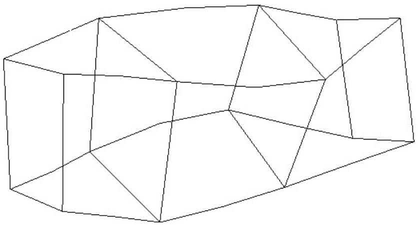

Figure 13: Free-Free half-scale chassis second torsional mode at 132 Hz.

4.3 Finite Element Damping Results

By applying a swept-sine forcing function from 0 to 200 Hz to the simulated structure at points where the stinger was attached to points on the frame, a frequency response function (FRF) may be generated. The step that controls the FRF output is a steady-state dynamics step with a frequency range from 20 to 150 Hz, allowing us to calculate the FRF for the whole range of interest. The force is applied at points 2 and 6 of the structure in the same direction as it was in the experiment. The FRF that was found is displayed in Figure 14. From the figure, the natural frequencies are shown as spikes. The spikes in this range are at 54, 86, 101, 132, and 144 Hz.

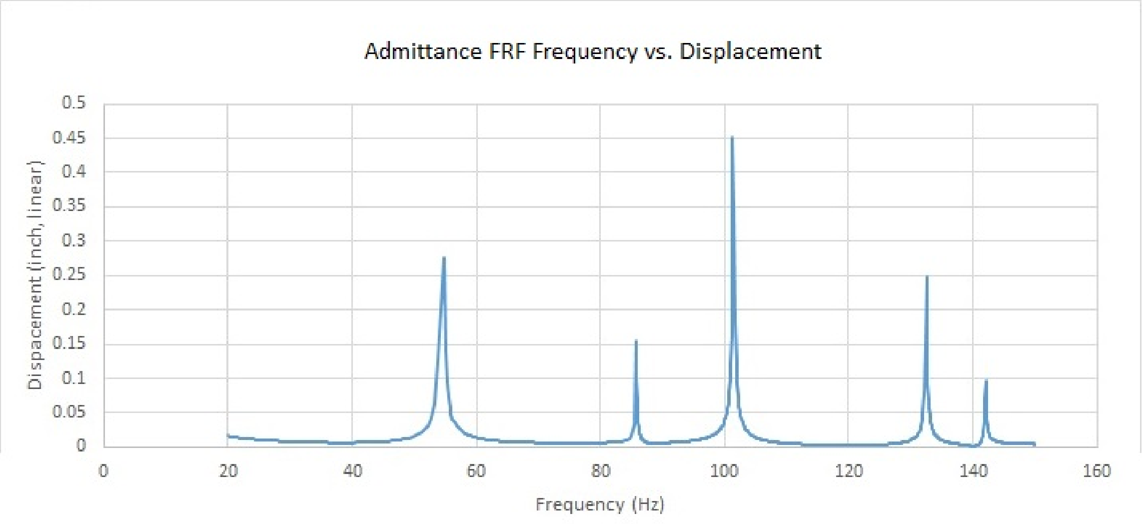

Figure 14: Admittance Frequency Response Function. Response at node 2 to displacement at node 6.

5 Half-Scale Discussion and Comparison of Results

Both the experiment and simulation of the half-scale chassis found natural frequencies. The experiment found more natural frequencies than the simulation, as shown in Table 5, but the errors, defined by Equation 7 generally less than 5%. Notice how some of the frequencies that the accelerometers register do not appear in the computer simulation. The paragraphs following the comparison will detail the analysis mode shapes at several of the natural frequencies to prove that the Abaqus simulation accurately represents the physical mode shapes of the system.

Table 5: Comparison between computational and experimental natural frequency calculations.

Computational (Hz)	Experimental (Hz)	% Difference
54.4	51	-6.75
	82.5	
85.8	86.75	1.15
91.1	93	2.04
101.4	100	-1.43
	108	
117.1	122	4.06
132.5	130	-1.90

$$\%\,Error = 100\left(\frac{Experimental - Abaqus}{Abaqus}\right) \tag{7}$$

The locations of the accelerometers are shown in Figure 15. The mode shapes studied with experiments are compared to the mode shapes from the simulations. For the 54/51 Hz mode shape, all of the accelerometers should have recorded motion. In fact, three of the accelerometers recognized nodes of the system at 51 Hz. For the 86 Hz case (the first shearing mode of the system), because there was only vertical and transverse motion, accelerometers directed laterally to the motion should not have recognized motion at all. The experiments found that this was the case, the nodes 1, 2, and 3 all displayed that there was a significant motion at 86 Hz, while the nodes 5, 6, 7, and 8 saw anti-resonance at this frequency. Node 4 did not have a phase change or peak at this frequency. This makes sense and is compatible with the computer simulations. The 132 Hz mode shape should have seen motion in all directions at this frequency. In this case, only six of the accelerometer positions correctly measured motion at this frequency.

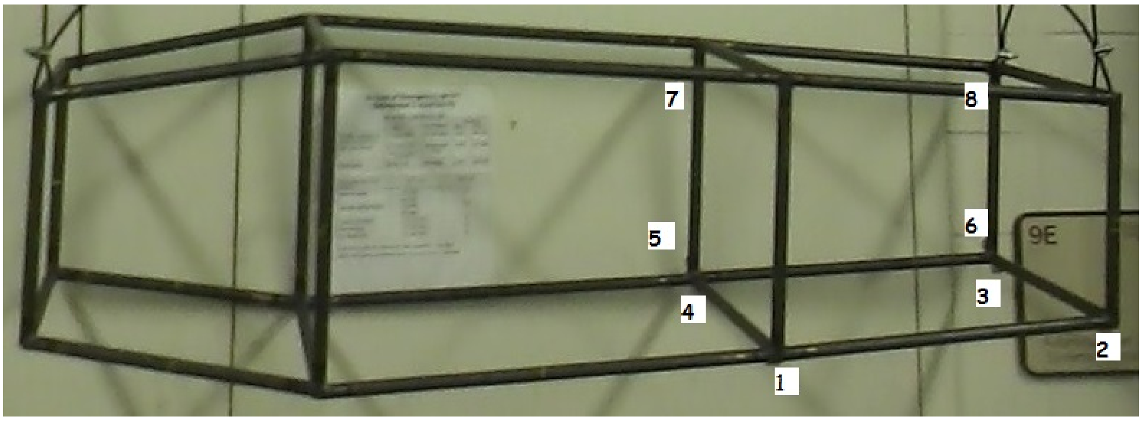

Figure 15: Numbered acceleration attachment points.

Potential for error was high in this analysis as there were several sources of error that may have occurred. Inaccuracies from the recording devices may be due to the placement of the accelerometer, as they were not directly on the joints, but slightly offset to ensure a strong bond with the frame. In addition, the direction of the accelerometer may be not quite perpendicular and this could could cause motion to be recorded when there should not be motion or vice-versa. A third option for the differences is that the stinger may have been slightly out of alignment, resulting in a force application in a different direction than expected. Overall the computer model showed good agreement with the experimental tests.

6 Composite Testing

6.1 Laminate Analysis

6.1.1 Coordinate Systems

There are two coordinate systems associated with a flat composite plate. The first is the ply coordinate system, which defines the individual ply, and the second is the local coordinate system, which defines how the ply fits in with the layup of the laminate as shown in Figure 16. In the ply coordinate system, the 1-direction correlates to the major fiber direction. The 2-direction is perpendicular to 1-direction and still within the plane of the laminate. The 3-direction is perpendicular to both and directed through the thickness of the laminate. In the local coordinate system, x, y, and z relate to how the laminate is placed in the structure. The x-, and y-directions are in the plane of the laminate, and z-direction is through the thickness of the laminate.

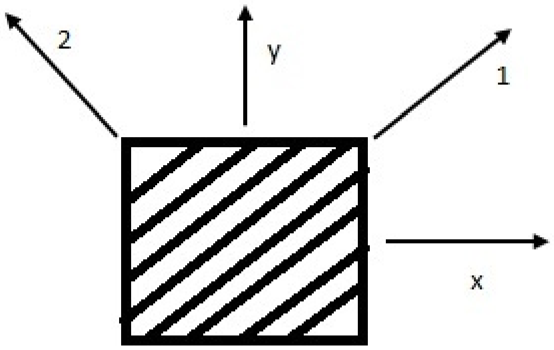

Figure 16: Definition of ply and local coordinate systems on a composite plate.

6.1.2 Assumptions

Several assumptions can be made for this analysis. The width and length of the laminated plate are greater than 50 times larger than the thickness of the laminated plate, meaning that Classical Lamination Theory (CLT) can be used instead of three-dimensional analysis or First Order Shear Deformation Theory. Because it is thin, Kirchoff's hypothesis can be used to simplify the analysis as well as the plane stress assumption [23].

6.1.3 Compliance and Stiffness Matrix

Stresses and strains have six components in this analysis. Each comprises three normal components and three shear components. The Plane-Stress assumption states that the stresses in the body can only be present in three of the components: σ_1, σ_2 and τ_{12}. Enforcing the Plane-Stress assumption results results in the Equation 8.

$$\left\{\begin{array}{c}\epsilon_1\\ \epsilon_2\\ \epsilon_3\\ \gamma_{23}\\ \gamma_{13}\\ \gamma_{12}\end{array}\right\} = \begin{bmatrix} S_{11} & S_{12} & S_{13} & 0 & 0 & 0\\ S_{12} & S_{22} & S_{23} & 0 & 0 & 0\\ S_{13} & S_{23} & S_{33} & 0 & 0 & 0\\ 0 & 0 & 0 & S_{44} & 0 & 0\\ 0 & 0 & 0 & 0 & S_{55} & 0\\ 0 & 0 & 0 & 0 & 0 & S_{66}\end{bmatrix} \left\{\begin{array}{c}\sigma_1\\ \sigma_2\\ 0\\ 0\\ 0\\ \tau_{12}\end{array}\right\} \tag{8}$$

The Plane-Stress assumption results in $\gamma_{23} = \gamma_{13} = 0$, allowing us to reduce the matrix from a 6x6 to a 3x3, and simplifying the required computations. This new 3x3 matrix in Equation 9 is called the "reduced compliance matrix" and the inverse is the "reduced stiffness matrix". Equation 10 is used for calculating strain in the 1-direction, the 2-direction and the 12-shear direction.

$$\begin{Bmatrix} \epsilon_1 \\ \epsilon_2 \\ \gamma_{12} \end{Bmatrix} = \begin{bmatrix} S_{11} & S_{12} & 0 \\ S_{12} & S_{22} & 0 \\ 0 & 0 & S_{66} \end{bmatrix} \begin{Bmatrix} \sigma_1 \\ \sigma_2 \\ \tau_{12} \end{Bmatrix} \tag{9}$$

and

$$\epsilon_3 = S_{13}\sigma_1 + S_{23}\sigma_2 \tag{10}$$

6.1.4 Transformation Matrix

So far, only the local coordinate system has been accounted for. In order to combine the properties of laminates, the matrices and stresses must be transformed to the global system in order to add one lamina to the next to make a laminate. The transformation matrix makes use of the angle difference from the x-direction of the laminate to the 1-direction of the ply. In the Equation 11, m=cos(θ), and n=sin(θ).

$$\begin{Bmatrix} \epsilon_1 \\ \epsilon_2 \\ \frac{1}{2}\gamma_{12} \end{Bmatrix} = \begin{bmatrix} m^2 & n^2 & 2mn \\ n^2 & m^2 & -2mn \\ -mn & mn & m^2-n^2 \end{bmatrix} \begin{Bmatrix} \epsilon_x \\ \epsilon_y \\ \frac{1}{2}\gamma_{xy} \end{Bmatrix} \tag{11}$$

By applying the transformation matrix to the previous compliance matrix in Equation 9 and stiffness matrix, the result is $\bar{S}$ and $\bar{Q}$ matrices, respectively. The $\bar{Q}$ matrix, which is the reduced and transformed stiffness will be particularly useful when developing the ABD Matrix in the following section.

6.1.5 Force and Moment Resultants/ABD Matrix

Kirchoff's Hypothesis assumes that the laminate layers are thin and perfectly bonded to one another so that no slipping can occur between lamina plies. The mid-surface of the structure is the center plane through the thickness. Kirchoff's Hypothesis states that the line normal to the mid-surface remains undeformed when stresses are applied. This means that no strains can exist in the z-direction, contrary to the Plane-Stress assumption. Displacements and curvatures which occur can be related to the normal and shear stresses through Equation 12.

$$\begin{Bmatrix} \sigma_x \\ \sigma_y \\ \tau_{xy} \end{Bmatrix} = \begin{bmatrix} \bar{Q}_{11} & \bar{Q}_{12} & \bar{Q}_{16} \\ \bar{Q}_{12} & \bar{Q}_{22} & \bar{Q}_{26} \\ \bar{Q}_{16} & \bar{Q}_{26} & \bar{Q}_{66} \end{bmatrix} \begin{Bmatrix} \epsilon_x^0 + z\kappa_x^0 \\ \epsilon_y^0 + z\kappa_y^0 \\ \gamma_{xy}^0 + z\kappa_{xy}^0 \end{Bmatrix} \tag{12}$$

The global strains have been broken up into their normal and curvature components, the global stresses can be modified to be represented by loads on the laminates. The loads on the structure will be represented by unit force and moment resultants on the laminated plate. The force resultants are force per unit length and the moment resultant are moments per unit length. The unit strains and curvatures can be also separated into ϵ and κ components. The matrix combining the force and moment resultants, the laminate configurations, and the reference surface deformations is shown in Equation 13, where the 6x6 matrix is referred to as the ABD matrix.

$$\begin{Bmatrix} N_x \\ N_y \\ N_{xy} \\ M_x \\ M_y \\ M_{xy} \end{Bmatrix} = \begin{bmatrix} A_{11} & A_{12} & A_{16} & B_{11} & B_{12} & B_{16} \\ A_{12} & A_{22} & A_{26} & B_{12} & B_{22} & B_{26} \\ A_{16} & A_{26} & A_{66} & B_{16} & B_{26} & B_{66} \\ B_{11} & B_{12} & B_{16} & D_{11} & D_{12} & D_{16} \\ B_{12} & B_{22} & B_{26} & D_{12} & D_{22} & D_{26} \\ B_{16} & B_{26} & B_{66} & D_{16} & D_{26} & D_{66} \end{bmatrix} \begin{Bmatrix} \epsilon_x^0 \\ \epsilon_y^0 \\ \epsilon_{xy}^0 \\ \kappa_x^0 \\ \kappa_y^0 \\ \kappa_{xy}^0 \end{Bmatrix} \tag{13}$$

Depending on the laminate configuration, this ABD matrix can have several coefficients equal to zero. The terms which will cause unwanted coupling and warping of the plates are the A16, A26, D16, D26 and the entire B matrix. The A16 and A26 elements couple extension and shear. D16 and D16 elements couple bending in either direction to twist. The B11, B12, and B22 elements couple extension in either direction with bending in either direction. B16 and B26 couple extension with warping and B66 elements couple shear with twist. Eliminating as many coupling components as possible is beneficial to the development of good laminates. Two special configurations which result in elimination of several elements of the matrix are balanced laminates and symmetric laminates.

Balanced laminates are those in which all layers other than zero and ninety degrees occur in ± pairs. Where, for every positively oriented lamina of a material property and thickness, there is one with the same material property and thickness but with a negative orientation somewhere in the laminate [24]. A balanced laminate eliminates the shear-extension coupling of the laminate, but does not remove the bending-twist coupling. The effect of using a symmetric, but unbalanced laminate is shown in Figure 17. The unwanted deformation which occurs is due to the extension-twist coupling inherent in a symmetric laminate.

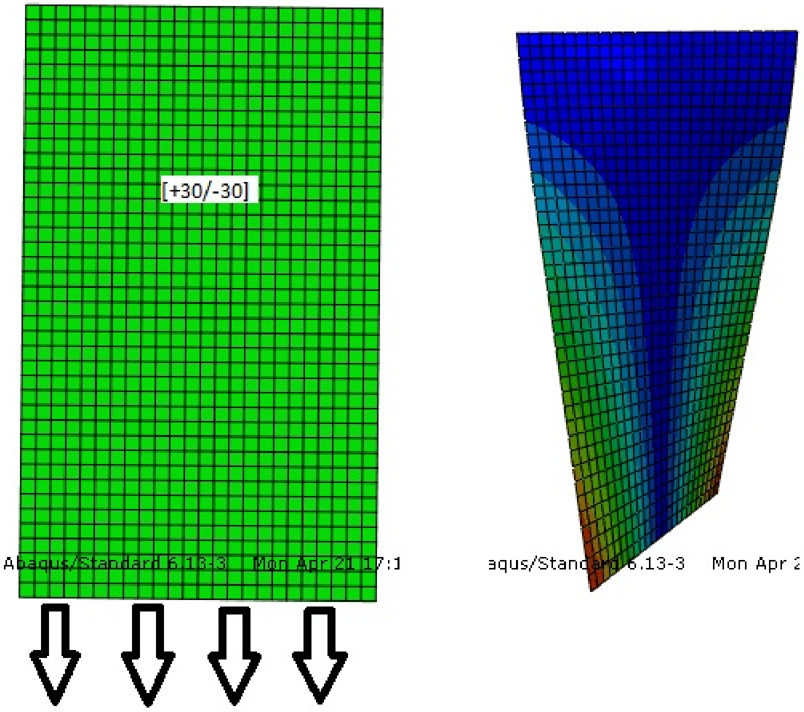

Figure 17: This figure shows the coupling from an extension force on a symmetric laminate. Red indicates a large amount of deformation and blue indicates very little to no deformation.

In a symmetric laminate, for every lamina of material property, thickness, and orientation lying a certain distance above the mid-plane of the laminate, there exists a lamina of the same material property, thickness and orientation lying the same distance below the mid-plane [24]. A symmetric layup will remove the bending-twist coupling present in general anisotropic laminates. A balanced and symmetric laminate would combine the effects of the balanced laminates and the symmetric laminates, but would still experience bend-twist coupling. The specific laminates analyzed in this work will be discussed in a later section of the thesis. For this work, balanced, symmetric laminates will be used which combine the best of both worlds, so that only D16 and D26 coupling elements remain nonzero.

6.1.6 Choice of Variables

From the composite property introduction, it is clear that many variables can be modified. The most common design variables include the individual ply geometry, ply thickness, stacking sequence, ply orientations, laminate thickness, location of the panels, and method of attachment. The chosen design variables are listed in Table 6. A large quantity of bi-axial woven carbon-fiber cloth was donated to the team; the individual ply and its construction cannot be changed. In addition, the attachment technique to the chassis is not within the scope of the project. The laminate stacking sequence and ply orientations, however, can be changed. In order to remove the coupling components from the system, the laminates will be both balanced and symmetric when they are four, six, or eight plies thick. When the laminate is only two plies thick, the structure will be symmetric.

Table 6: Chosen design variables and bounds.

Design Variables	Lower Bound	Upper Bound
Ply orientation (degrees)	-90	90
Stacking sequence	Symmetric only	Balanced and Symmetric
Laminate thickness (number of plies)	2 plies	8 plies

6.2 Composite Tensile Test Setup

The composites used for the analysis will be tested to determine material properties. The outlined procedure will be performed in accordance with ASTM D3039 standards. The results of the testing will be discussed, and the corresponding engineering properties of the composite will be determined. This standard deals with standard test methods for tensile properties of polymer matrix composite materials. These standards designate the apparatus to be used as well as the testing procedures.

The carbon-fiber cloth tested in this project was donated by the company Composite Fabrics of America. They generously supplied the Formula SAE team with 75 yards of 3K carbon-fiber fabric with a density of 197gsm ($5.7oz/yd^2$). Tensile tests were completed to estimate accurate material properties for the 8-ply 0-90 coupons. Resin was pushed into the carbon-fiber fabric, smoothed, and then covered with a vacuum bag for 24 hours to remove the resin. There was a malfunction with the vacuum bag during this process that resulted in a heavy resin layer on the surface of the composite that required sanding. Upon curing, the plate was cut into fifteen ten inch by one inch coupons (10"x1") for tensile testing analysis. Five coupons were made for each orientation: zero degrees, ninety degrees and forty-five degrees. The cross sections of these coupons showed little to no instances of voids; however, due to the hand layup process, extra resin may have deteriorated the carbon-fiber panel's strength. The testing process and the results gathered are discussed below.

6.3 Alignment Procedure and Results

ASTM document D3039M-09 [2] discusses in detail the method for determining the alignment of the Instron load frame. The method involves using three strain gages in the center of the specimen (two on one side and one on the other) to determine bending around two axes of the structure, as shown in Figure 18. In this case, the coupon is a zero-degree piece of composite that is cut from the same material as the coupons for later tensile testing as required by ASTM D3039 [2].

In order to determine the alignment, the zero strain point was taken after the specimen had been clamped in the structure. To achieve friction between the grips and the coupon, two inches of both ends of the test coupon were covered in 100x100 stainless steel mesh and then further covered with a four inch strip of deadsoft aluminum (thickness .032 inches) bent in half around the coupon. During clamping, an Instron load frame feature called "specimen protect" was used to keep the loads on the coupon low by moving the head incremental amounts. Following clamping, the strain at all three axial strain gages was monitored until a strain of greater than 500 micro-strain [2] was measured by all three gages. The data was recorded and then the specimen is rotated 180 degrees. Tests were performed in a total of four configurations - upright, upside down, reversed, reversed upside down - so that each direction was checked. The four data sets were then checked to determine the percent bending around the y- and z-bending axes of the system by Equations 14 and Equation 15, respectively.

$$By = 100 \times \frac{\epsilon_{ave} - \epsilon_3}{\epsilon_{ave}} \tag{14}$$

$$Bz = 100 \times \frac{\frac{2}{3}(\epsilon_2 - \epsilon_1)}{\epsilon_{ave}} \tag{15}$$

where:
By = percent bending of the system about the narrow plane
Bz = percent bending of the system about the wide plane
$\epsilon_1, \epsilon_2, \epsilon_3$ = longitudinal strains on gages SG1, SG2, and SG3, respectively, as identified in Figure 18.
$\epsilon_{ave} = ((\epsilon_1+\epsilon_2)/2+\epsilon_3)/2$

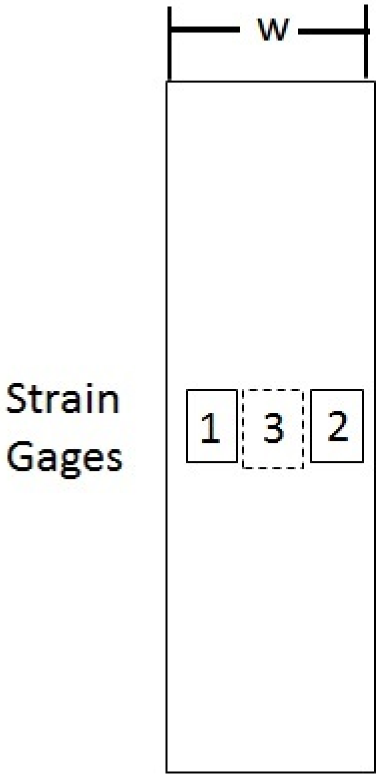

Figure 18: Gage locations for the system alignment check coupon. This figure was based off one in the ASTM D3039 Standard [2].

The results for the alignment procedure are shown in Table 7. ASTM D3039 suggests that the alignment of the testing apparatus is to be between three and five percent. The bending about the narrow plane of the structure averages 1.5 percent while the bending about the wide plane of the structure is 6.44 percent. While the bending about the wide plane is slightly out of the range specified, it should not impact the results achieved significantly as the wet-layup process used results in resin inconsistencies that will overshadow a 1.44 percent bending above the allowable in the testing apparatus.

Table 7: Bending values for percent alignment

Alignment	1	2	3	4	Average
By	0.865	1.930	1.279	1.955	1.507
Bz	7.723	10.37	2.158	5.529	6.445

6.3.1 Tensile Procedure

The testing machine follows the requirements laid out, in that there is one stationary and one movable head. The grips on the testing machine have the ability to hold the composites properly; however, the composites must be tabbed [2] in order to make sure the grips hold onto the composites without damaging the individual fibers. The ends of the composites in the tests were first covered with a stainless steel 100 x 100 mesh and then 4 inches of .032 inch deadsoft aluminum was bent around the mesh. The tabs allow the load frame grips to attach to the aluminum and dig into the mesh, thereby holding on to the composite without damaging individual fibers. The Instron load frame utilizes a specimen protect option that keeps the load below 50 lbfs while gripping the specimen by moving the crosshead in incremental amounts. The zero strain point is taken after the fibers have been gripped resulting in clear data from a zero load state.

The specimens that have been used are rectangular in shape [2] with dimensions of 10 inches long by 1 inch wide. The specimens were flat, and a few exhibited a lack of resin in some areas which caused them to fail at earlier stress values. The tabs used to grip the specimens extended two inches from the ends of the coupon towards the center on both sides of the specimens, and did not cause failure at the points where they were gripped in the load frame. The specimens were measured for width, thickness and length using a micrometer at five points as shown in Figure 19. The top side of the specimen as shown has 2 equally spaced points, approximately 3.33 inches from each edge and each other. The bottom side of the specimen in the figure has 3 equally spaced points, approximately 2.5 inches from each other and the edges. The five measurements are averaged to determine the width and thickness used in future calculations. The width is multiplied by the depth (thickness) to determine the average cross sectional area of the specimen. The length of the specimen was measured as well and the measured geometry for each specimen is given in Appendix D.

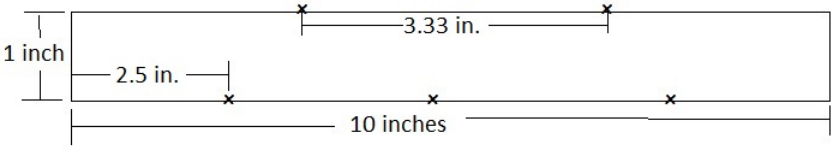

Figure 19: Positions for micrometer measurement to determine width and thickness

The speed of the constant cross-head tensile tests will be set at .05 in/min as stated by the ASTM D3039 standard [2]. In addition, the ultimate values were recorded for specimens which break at obvious flaws(such as extra resin, lack of resin, large voids, ect.). The fracture methods were recorded for all specimens and correspond to standard fracture methods shown in ASTM D3039 [2]. Analysis of the data after testing is conducted and the stress and strains at all data points are determined with Equations 16 and 17, respectively.

$$\sigma = P/A \tag{16}$$

$$\epsilon = \delta/L_g \tag{17}$$

where:
σ = Tensile stress at ith data point (psi)
P = Force at ith data point (lbf)
A = Average cross sectional area (in^2)
ϵ = Tensile strain at ith data point (in/in)
δ = Extensometer displacement at ith data point (in)
L_g = Extensometer gage length (in)

The tensile chord modulus of elasticity either E1 or E2 is determined from the stress strain graph and is reported to three significant figures. The Poisson's ratio is also determined for the specimens and reported to three significant figures. Equations 6.3.1, and 19 show the method of determining the the Tensile Modulus and the Poisson's ratio from the data.

$$E^{chord} = \delta\sigma/\delta\epsilon \tag{18}$$

where:
E^{chord} = Tensile chord modulus (psi)
$\delta\sigma$ = Difference between applied stress at two different data points (psi)
$\delta\epsilon$ = Difference between strain at the same two different data points (in/in)

$$v = -\delta\epsilon_{lat}/\delta\epsilon_{long} \tag{19}$$

where:
ν = Poisson's ratio
ϵ_{lat} = difference in lateral strain between two longitudinal strain points (in/in)
ϵ_{long} = difference between two longitudinal strain points (in/in)

7 Tensile Test Results

Tensile tests were conducted between 2/20/2014 and 2/28/2014 according to the ASTM 3039 standards [2]. Eleven samples were tested with strain gages. Each sample comprised eight woven bi-directional layers, all of which were oriented the same direction. Samples were cut from the material at zero-, forty-five- and ninety-degree orientations for testing to gather the relevant material data. The samples had average geometric properties shown in Table 8. The width and thickness of each test coupon was measured at five locations in each specimen as shown in Figure 20. The specimens were tabbed as described previously, and tested with the Instron load frame. The geometric details of each specimen is detailed in Appendix D.

Table 8: Composite coupon specimen dimensions

Property	Width (in)	Thickness (in)	Length (in)
Average	0.999	0.143	9.99
Std Dev	0.0176	0.00407	0.0481

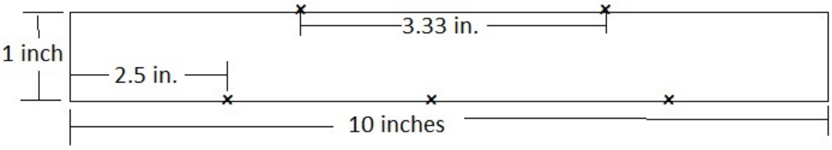

Figure 20: Micrometer measurement positions to determine width and thickness.

7.1 Determined Properties

Four zero-degree coupons were tested in tension. The average E_1 of the material was found to be 4.53 Mpsi ±.178 Mpsi. Where the ± establishes one standard deviation above and below the average value. While most carbon-fiber reinforced laminates have E1 values on the order of 10 Mpsi, due to the out of autoclave wet layup process for the tested material, the strength is much lower than expected. There were also problems in the layup of this particular sheet, that resulted in resin remaining on the surface of the structure as shown in Figure 21. The resin was sanded off prior to testing using wet sand paper and resulted in a smooth surface with a variation in thickness less than the ±4% of the thickness that the ASTM D3039 standard [2] designates. The Poisson's ratio, ν_{12}, was determined to be approximately .0667.

Two of the zero-degree coupons utilized a single axial strain gage as opposed to a Poisson's gage, resulting in a lack of gathering of the Poisson's ratio. The failure mode displayed in Table 9 is shown as is recommended in the ASTM standard. The mnemonic, LGM, refers to the failure occurring Laterally, in the Gage section in the Middle of the specimen. The mnemonic, LAT, represents failure that occurred Laterally, at the Grip and at the Top of the specimen. The mnemonic, AGM, represents failure which occurred in an Angular direction, in the Gage section in the Middle of the specimen. The test specimens, post failure are shown in Figure 22.

Table 9: Determined engineering properties of the zero-degree directional coupons

Orientation and Label	E_1 (psi)	ν_{12}	$\sigma_{1,max}$ (ksi)	$\epsilon_{1,max}$ (in/in)	Failure Mode
0-1	4.75E+06	0.0501	39.8	0.00835	LGM
0-2	4.60E+06	0.0833	39.1	0.00850	LGM
0-3	4.39E+06	N/A	35.3	0.00810	LAT
0-4	4.38E+06	N/A	35.4	0.00799	LGM
Average	4.53E+06	0.0667	37.4	0.0082359	
Standard Dev.	1.78E+05	N/A	2.41	2.31E-04	

Figure 21: Wet layup resulted in resin remaining on the surface of the panel, potentially reducing the overall strength.

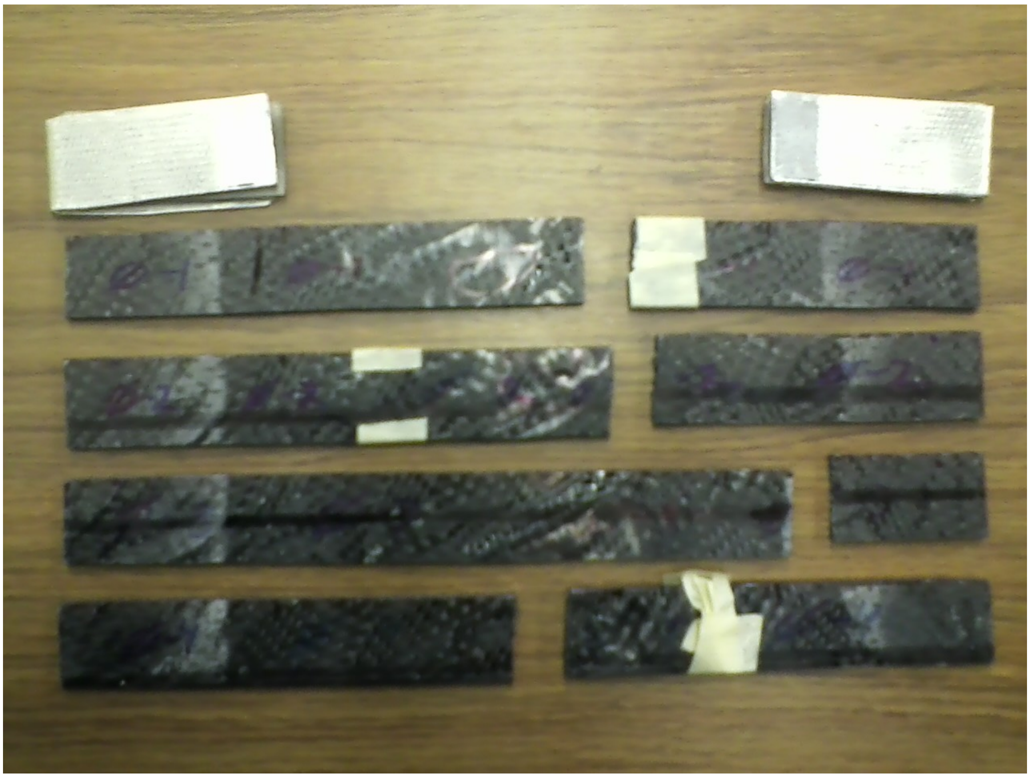

Figure 22: Zero-degree specimens post failure: break is lateral, as expected.

Three ninety-degree specimens resulted in usable data, and are shown along with the averages and standard deviations in Table 10. The average E_2 of the material is found to be 4.67 ± .078 Mpsi. The value of E_2 is 3.1 percent higher than the value of E_1. In addition, the maximum stress from these specimens are 3.5 percent different than the zero-direction fibers. The result from the zero and ninety-degree directional fiber tests shows that the bi-axial woven cloth is quite symmetric. The failed ninety-degree test coupons are shown in Figure 23.

Table 10: Determined engineering properties of the ninety-degree directional coupons

Orientation and Label	E_2 (psi)	ν_{21}	$\sigma_{2,max}$ (ksi)	$\epsilon_{2,max}$ (in/in)	Failure Mode
90-2	4.67E+06	0.0614	42.2	0.00902	LAT
90-3	4.60E+06	0.0580	38.6	0.00846	LGM
90-4	4.75E+06	0.0250	35.5	0.00796	LGM
Average	4.67E+06	4.81E-02	38.7	8.48E-03	
Standard Dev.	7.80E+04	2.01E-02	3.38	5.27E-04	

Figure 23: Ninety-degree specimens post failure: break is lateral as expected

The forty-five-degree fiber orientation results are shown in Table 11. The average modulus with this orientation is determined to be 1.11 ± .0405 Mpsi, and the Poisson's ratio is approximately .8. The coupons were tested at a rate of .25 in/min due to the larger deformations involved. The maximum deformation was just over 10x higher for the forty-five-degree coupons due to the scissoring effect from the realigning of the fibers. This effect is seen in the specimens after failure in Figure 24.

Figures 25, Figure 26, and Figure 27 show the stress vs strain curves associated with each orientation. The zero and ninety-degree orientations are very similar and quite linear with Young's Modulii of 4.52 and 4.67 Mpsi, respectively. The forty-five-degree orientation can withstand 10x more strain than the other two; however, the maximum stress is a 16.3 ksi, a factor of 2.3 lower than either the 1- or 2-directions. The samples of each coupon group show similar trends, and maximum values.

Table 11: Determined engineering properties of the forty-five-degree directional coupons

Orientation and Label	G_{12} (psi)	Poisson	$\sigma_{12,max}$ (ksi)	$\epsilon_{12,max}$ (in/in)	Failure Mode
45-2	1.13E+06	0.812	16.5	0.103	AGM(2)
45-3	1.06E+06	0.787	16.0	0.113	AGM(2)
45-4	1.14E+06	0.797	16.5	0.0949	AGM(2)
Average	1.11E+06	7.99E-01	16.3	1.04E-01	
Standard Dev.	4.05E+04	1.31E-02	3.09E-1	8.98E-03	

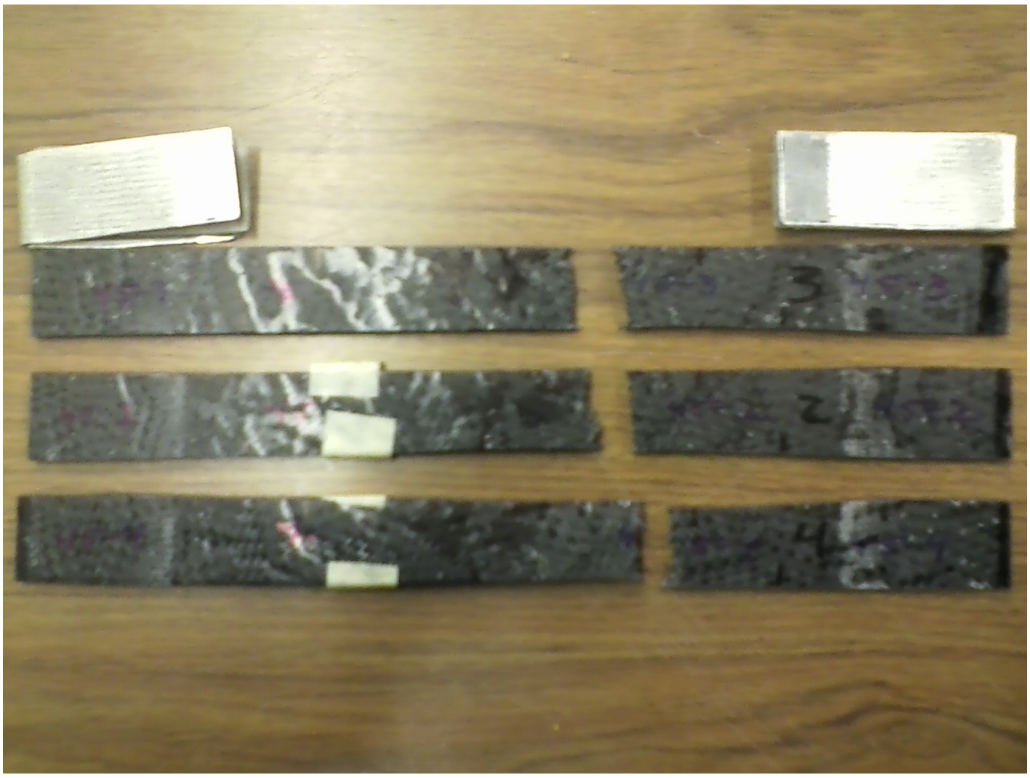

Figure 24: Forty-five-degree specimens post failure: break displays scissoring, as expected

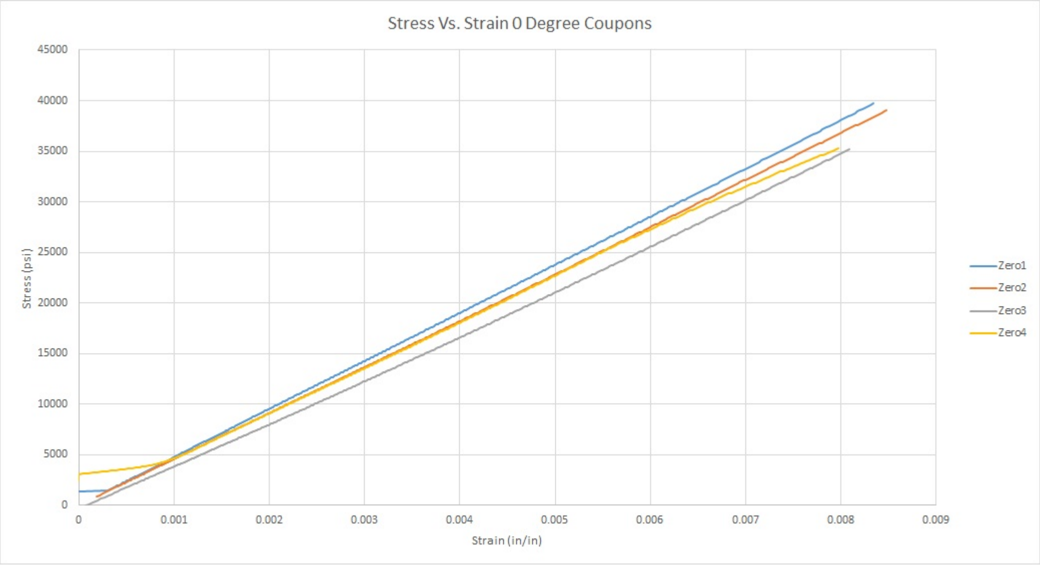

Figure 25: A nominal stress vs. nominal strain graph as measured by the strain gages for the zero-degree test coupons.

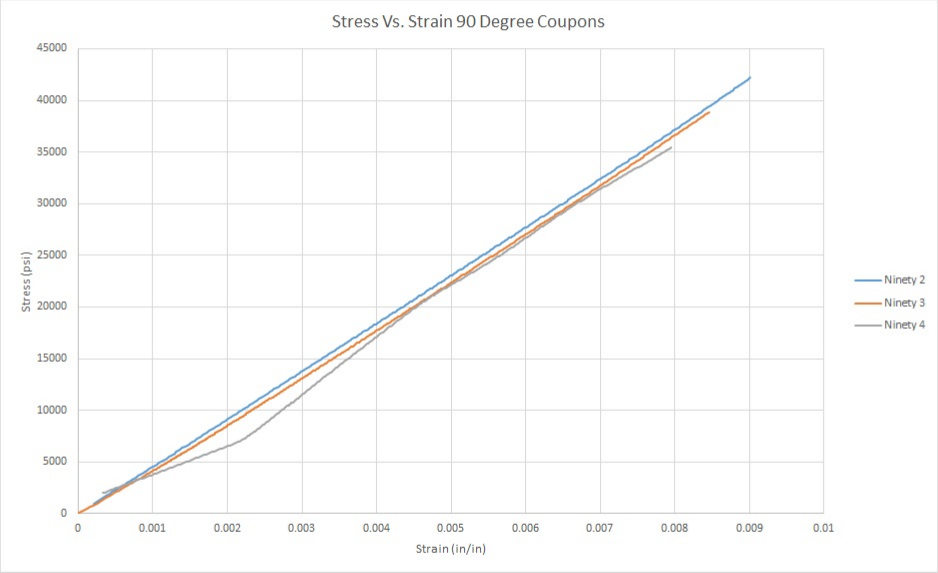

Figure 26: A nominal stress vs. nominal strain graph as measured by the strain gages for the ninety-degree test coupons.

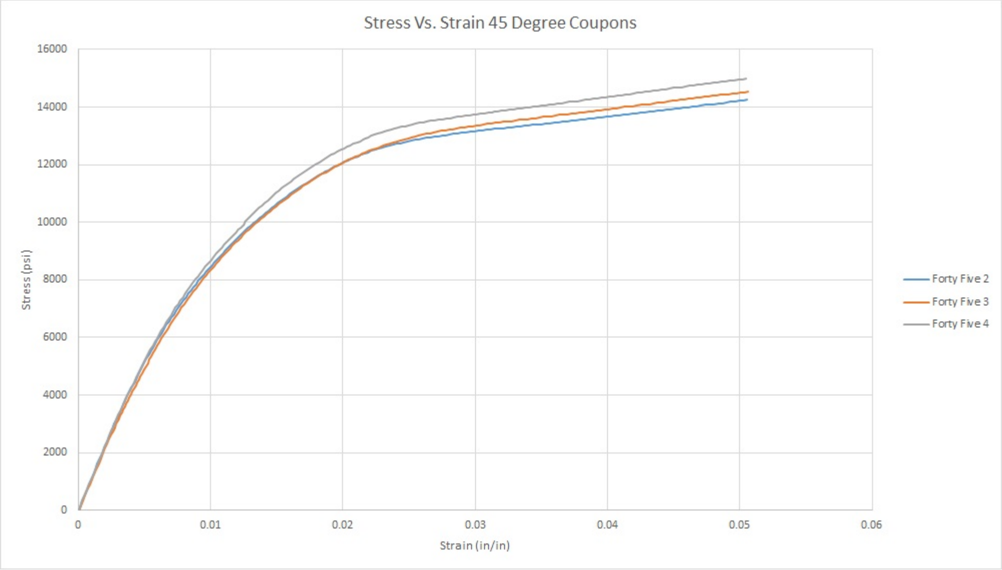

Figure 27: A nominal stress vs. nominal strain graph as measured by the strain gages for the forty-five-degree test coupons. The gages broke before the maximum strain of the sample was reached.

8 Abaqus Composite Analysis

Material property data shown in Table 12 for the composite material has been gathered from testing composite specimens in the Instron load frame and input into the Abaqus finite element program. The finite element representation of the 10x1 inch composite specimen developed in Abaqus is shown with boundary conditions and applied load in Figure 28. The left fixed boundary condition represents one gripped end of the specimen attached to the load cell. The right end of the coupon is constrained by the grips attached to the crosshead of the load frame. The mesh with which the element is made has been converged to .01% and the stress values and error convergence are shown in Figure 29. The mesh comprises Abaqus S4R elements which have four nodes, reduced integration and the aspect ratio of each undeformed element is one. The resulting mesh of 160 elements is shown in Figure 30.

Table 12: Material property data from composite specimen testing

Woven [0/90]s composite	Value	Units
E1	4.53	Mpsi
E2	4.67	Mpsi
ν	.012	N/A
Lamina Thickness	0.0667	in
Maximum Strain	0.0108	in/in
Maximum Stress	71.8	ksi

Figure 28: Simulated composite specimen with fabric weave oriented in a 0-90 configuration. Load applied in the 1-direction.

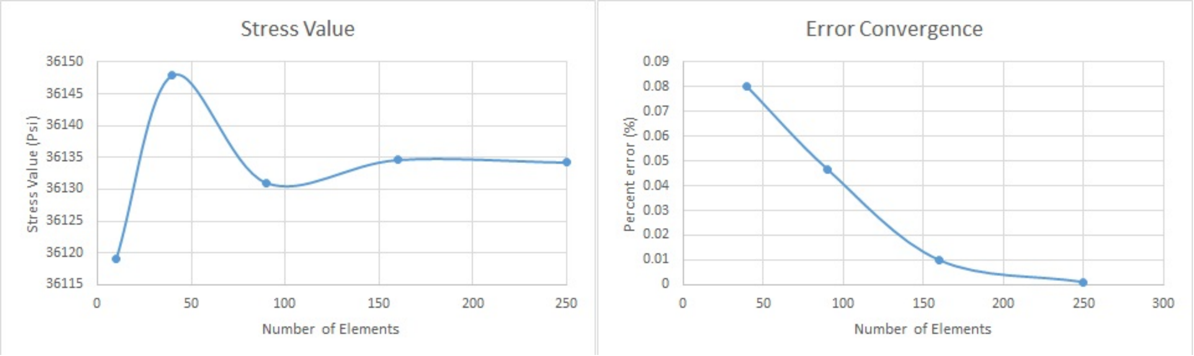

Figure 29: The stress convergence and the percent error associated with each step.

Values computed from the Abaqus composite code has been calculated at strain values ranging from 0 to .08 in/in. The comparison between the experimental stress vs. strain graphs and the simulated stress vs. strain graph is shown in Figure 31. The difference between the tested Young's Modulus and the simulated Young's Modulus is negligible, however the stress values at each tests strain is biased high. The systemic error in stress at strain values ranging from .008 to .08 in/in is shown in Table 13. The

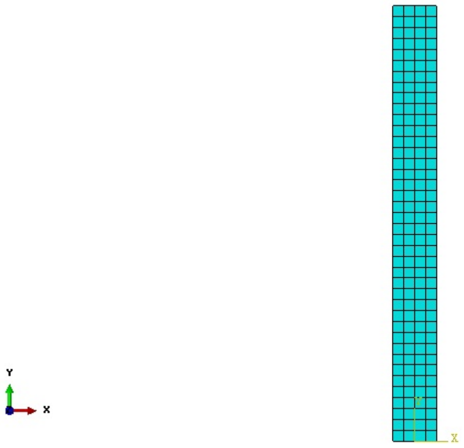

Figure 30: The chosen composite specimen finite element mesh.

sum of the percent error from all of the steps is fifteen percent, where error is calculated using Equation 20, which may potentially adversely effect later analyses.

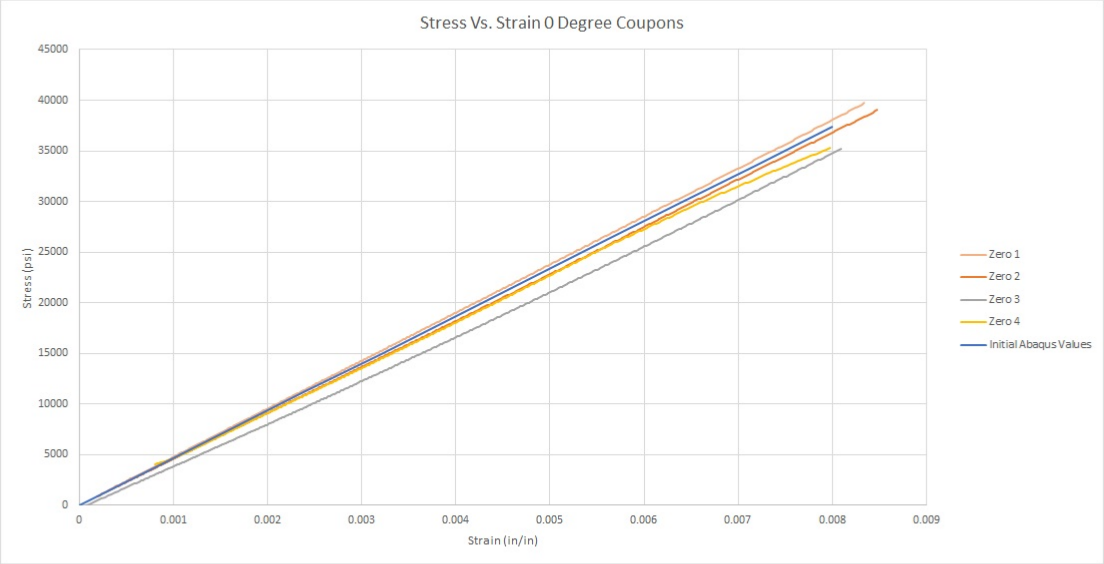

Figure 31: Comparison between the Young's Modulus of the simulation and the experiment.

$$Error_1 = 100(\frac{(Model_1 - Experimental_1^1)}{Experimental_1^1} + \frac{(Model_1 - Experimental_1^2)}{Experimental_1^2} + ... + \frac{(Model_1 - Experimental_1^4)}{Experimental_1^4}) \tag{20}$$

In order to determine correct property values to be used in Abaqus, the optimization code will determine the correct material properties to simulate the material. A simulated composite specimen was built in Abaqus and subjected to ten, equally spaced, incremental strains from 0 to .08 in/in and the resulting stresses measured, at locations far from the boundary and loading conditions to reduce interference. The ten strain quantities were compared to the equivalent strains of the four tested samples and the absolute value of the error was summed. The absolute value of the sum of the ten errors was minimized so that the stress strain curve approached the values determined from the testing situation. The set of minimization equations are shown below in Equations 21, 22, and 23.

$$Minimize f(x) = AbsoluteValue(Sum(Error_1 + Error_2 + ... + Error_{10})) \tag{21}$$

$$0psi < E1 < 30e6psi \tag{22}$$

Table 13: Biased-high systemic stress error in the Abaqus simulation

Strain (in/in)	Error Value (psi)	Percent Error
0.0008	-3.20E+01	-.883
0.0016	3.86E+02	5.33
0.0024	4.39E+02	4.04
0.0032	6.53E+02	4.50
0.004	4.88E+02	2.69
0.0048	7.54E+02	3.47
0.0056	-1.55E+02	-.611
0.0064	-4.15E+02	-1.43
0.0072	-3.75E+02	-1.15
0.008	-1.91E+02	-.527
Sum	1552	15.42672

$$0psi < E2 < 30e6psi \tag{23}$$

The value determined for the initial E_1 and E_2 result in an objective function value of 1552 psi. Following the optimization, the objective function has a value of just 16 psi. The error has also been reduced from 15.4% to 7.56%. The resulting values from the optimization are shown in Table 14 and show that: $E_1 = 4.52e6$ psi and $E_2 = 4.82e6$ psi. The optimization showed that from the initial assumption there was a .29 percent error of E_1 and a 3.14 percent error associated with E_2. The comparison between the initial and final properties as shown on a stress vs strain graph is shown in Figure 32. The error associated with the new properties is much lower and is shown numerically in Table 15.

Table 14: Material property data from composite specimen testing

Woven [0/90]s composite	Value	Units
E1	4.52	Mpsi
E2	4.82	Mpsi
ν	.0667	N/A
Lamina Thickness	0.0178475	in
Maximum Strain	0.0108	in/in
Maximum Stress	71.8	ksi

Table 15: Zero-bias systemic stress error in the Abaqus simulation following material property optimization.

Strain (in/in)	Error Value (psi)	Percent Error
0.0008	-6.00E+01	-1.66
0.0016	3.26E+02	4.51
0.0024	3.55E+02	3.27
0.0032	5.37E+02	3.72
0.004	3.48E+02	1.93
0.0048	5.82E+02	2.68
0.0056	-3.55E+02	-1.40
0.0064	-6.43E+02	-2.22
0.0072	-6.31E+02	-1.94
0.008	-4.75E+02	-1.31
Sum	-16	7.569061

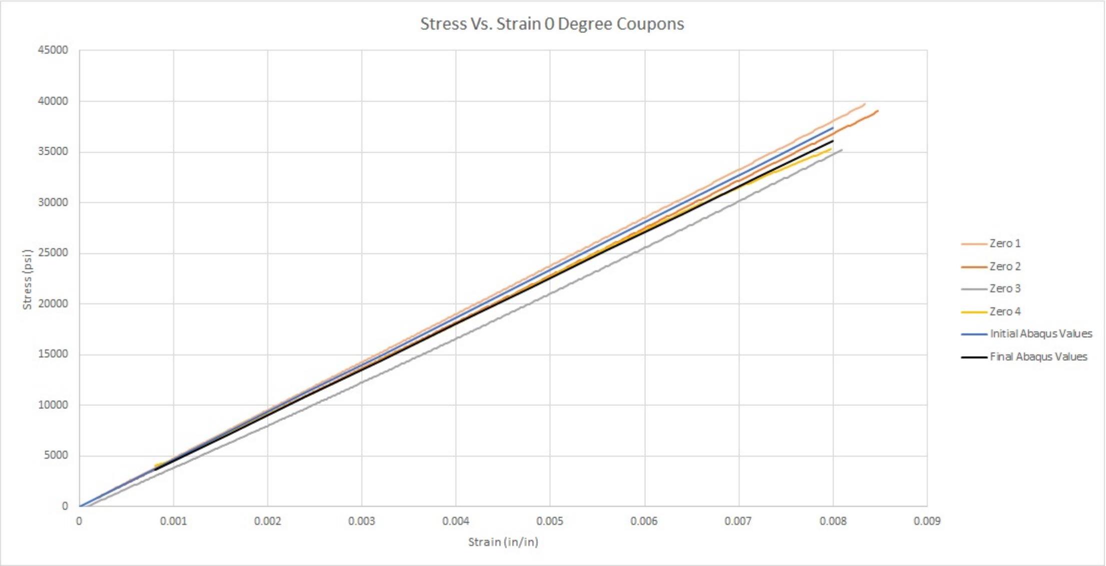

Figure 32: Nominal stress vs. nominal strain initial and optimized material properties. The black line of the final material property is situated in the center of the grouping.

9 MATLAB Optimization

This section discusses how the optimization code was developed and executed to optimize composite laminate configuration.

The essential variables or parameters to the optimization code were identified by evaluating the range of variables and then systematically removing variables until the essential variables remain. The two categories of potential parameters are material parameters and geometry parameters. The material parameters identified are: material properties (Young's modulus, Poisson's ratio, etc.), ply thickness, weave, resin, and curing method. The geometrical properties identified are: ply orientation/stacking sequence, panel geometry, panel connection to the chassis, overall thickness (weight). For this work, none of the material variables were changed, as such they are material parameters. The only geometrical parameter which cannot be changed is the shape of the panel, as it must correspond to the shape of the chassis section to which it attaches. The design variables were narrowed down to the individual ply orientations, stacking sequences, and the overall thickness of the panel. The overall panel thickness may be changed by adding or removing plies in the stacking sequence. The stacking sequences were further constrained as follows: when using two plies the layup is symmetric,and when using four, six and eight plies, the layup is balanced and symmetric.

A balanced stacking sequence means that for every ply of a material property, thickness, and orientation, there is a ply somewhere else in the laminate which has identical material properties and thickness, but with a negative orientation. A symmetric stacking sequence means that for every ply of a material property, thickness, distance from the midsurface, and orientation on one side of the midsurface of the composite, there is an identical ply on the opposite side at the same distance from the midsurface. When cut along the midsurface, the two pieces mirror each other. Building a balanced and symmetric laminate provides benefits in both manufacture and use of the composite. The benefits stem from the ABD matrix of the laminate. When the laminate is balanced and symmetric, the B matrix and the A_{16} and A_{26} components are all equal to zero. The zero components of the matrix decouples extension-twisting, as well as extension-shear. Because the D_{16} and D_{26} components are not zero, bending and twisting are still coupled.

The composites being used for the development of the panels of the chassis are woven composites. From measurements during testing, it is known that 8 layers of the woven composite will have a nominal value of 0.143 inches thick, and each layer is nominally 0.0179 inches thick. This single layer dimension was used in the Abaqus Composite Analysis section of the report. If the stacking sequence needs to be balanced and symmetric, the minimum balanced and symmetric laminate build must be $[+\theta/\text{-}\theta/\text{-}\theta/+\theta]$, where θ is a given ply orientation relative to the local panel coordinate system, and the minimum thickness would then be 0.0714 inches. The potential stacking sequences of the carbon fiber structures are shown in Table 16.

Table 16: Composite layup stacking sequences by number of plies

Number of Plies	Layup	Example Layup (degrees)
2	$[+\theta/\text{-}\theta\ ]$	[20/-20]
4	$[+\theta/\text{-}\theta\ ]_s$	$[20/\text{-}20]_s$
6	$[+\theta/\text{-}\theta/0\ ]_s$	$[20/\text{-}20/0]_s$
8	$[+\theta/\text{-}\theta/+\phi/\text{-}\phi\ ]_s$	$[20/\text{-}20/35/\text{-}35]_s$

9.1 Method

MATLAB was used to optimize the composite panels' orientation and number of plies. The composite panels were optimized to reduce overall chassis weight, increase stiffness, and reduce the sensitivity associated with the orientation angle, so that any defects which may occur during manufacturing will not have a significant negative impact on the vehicle's performance. The stiffness per unit mass was measured by determining the first natural frequency for transverse bending, lateral bending, and the first torsional modes of the system.

The MATLAB programs are provided in Appendix E of this report. MATLAB was used to randomly initialize the ply layup of an input file in Abaqus. The program calls Abaqus and extracts the requested frequency data from the Abaqus output files. The first torsional, lateral and transverse bending frequencies were normalized to the corresponding natural frequency of the steel space frame chassis. Over several iterations, the orientation resulting in the highest summed normalized natural frequencies was determined. The optimum ply orientation angle was then calculated by minimizing F in Equation 24. The original steel structure has an objective function value of negative three.

$$Minimize\,F(x) = F(\theta, \phi, number\,of\,plies) = -\frac{F_{bend1}}{F_{st,bend1}} - \frac{F_{bend2}}{F_{st,bend2}} - \frac{F_{tors}}{F_{st,tors}} \tag{24}$$

$$0\,degrees < \theta, \phi < 90\,degrees \tag{25}$$

$$number\,of\,plies = 2, 4, 6, 8 \tag{26}$$

where:
F = Objective function
θ = Ply orientation in the bottom of the structure (degrees)
ϕ = Ply orientation of the side panels of the structure (degrees)
F_{bend1} = First bending natural frequency at the ith orientation angle (Hz)
F_{bend2} = Second bending natural frequency at the ith orientation angle (Hz)
F_{tors} = First torsion natural frequency at the ith orientation angle (Hz)
st = associated frequency of the steel frame chassis (Hz)

10 Full Chassis Design

This section of the work discusses the geometry of the VT FSAE car chassis and the original stiffness and natural frequencies. The coordinate system for the chassis is the established SAE vehicle coordinate system and several views of the completed chassis are presented. The profiles of the tubes used in the construction of the chassis are provided. The first three natural frequencies: the first torsional natural frequency, the first lateral bending natural frequency and the first transverse bending natural frequency are determined. Following that, the integrated carbon-fiber panels are integrated into the chassis, the composite local coordinate systems are developed, and the different ply layups that are measured are discussed.

10.1 Coordinate System

The coordinate system of the chassis is the SAE vehicle coordinate system [25]; it is Cartesian XYZ right-handed coordinate system. The coordinate system used is shown alongside the model of the steel frame of the chassis in Figure 33. The SAE coordiante system defines the X-axis along the length of the car from the rear to the front. The Y-axis runs horizontally through the width of the car. The Z-axis is in the downward direction. This is the coordinate system used for the remainder of the work unless specified otherwise.

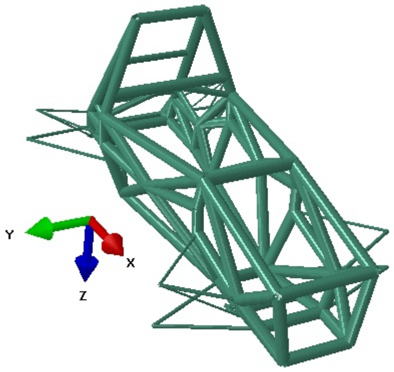

Figure 33: The coordinate system used for the chassis.

10.2 Original Chassis

The steel frame chassis is fabricated from 1" OD round structural tubing of various wall thicknesses. Front, side, and isometric views of the chassis are shown in Figures 34, 35, and 36, respectively. The chassis consists of three sections which are labeled in Figure 35. The rear bay extends from the rear of the car to the main rollhoop. The second section is the middle bay (cockpit bay), and is defined by the main roll hoop and the front roll hoop. The third section is the front bay, is defined by the front bulkhead and the front roll hoop. The steel tube cross section dimensions of the chassis, as they relate to the colors in Figure 36 are listed in Table 17. The material properties of the steel tubes used to fabricate the chassis are shown in Table 18. It is not within the scope of this work to change these steel frame nodal coordinates, however, as the composite become more integral to the structure in the future, it will become necessary to decrease the size and change the location of several tubes to save weight.

Table 17: Tube dimensions associated to the color in Figure 36.

Maroon	1" x 0.095"
Orange	1" x 0.065"
Blue	1" x 0.049"
Yellow	1"x 0.035"
Teal	1" x 0.028"
Pink	1" x 1" x 0.035" square tube
Purple	5/8" x 0.035"

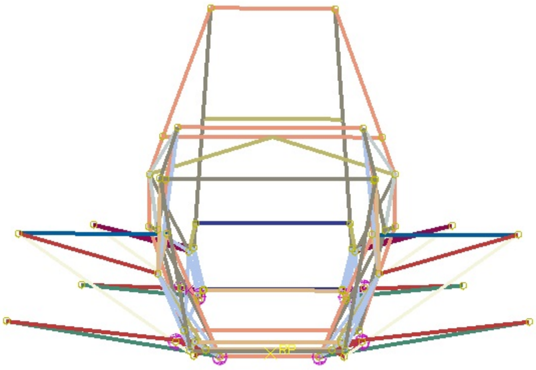

Figure 34: A front view of the original chassis.

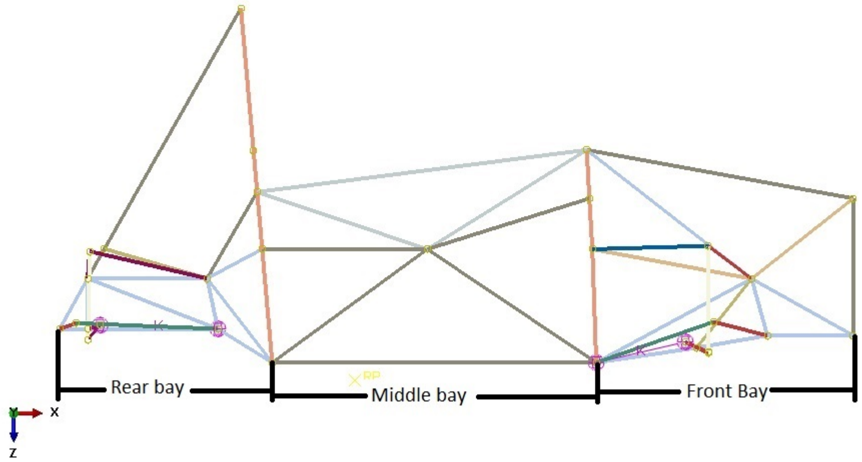

Figure 35: A side view of the original chassis.

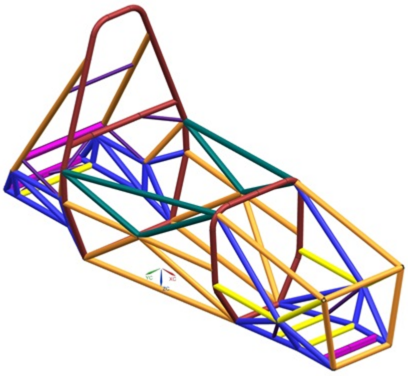

Figure 36: An isometric view of the different tubes which make up the chassis according to Table 17.

Table 18: Material properties of the steel in the space frame.

Material name	Normalized 4130 Steel
Youngs Modulus, E	30 Mpsi
Yield strength, S_y	44.2 ksi
Ultimate Tensile Strength, S_{ut}	52.9 ksi
Yield strength, welded, $S_{y,welded}$	26.1 ksi
UTS welded, $S_{ut,welded}$	43.5 ksi
UTS shear, S_{su}	31.8 ksi

The majority of the loads and boundary conditions which affect the chassis were input at the chassis hard points. These points are connected to the frame by way of control arms, pull rods and a suspension spring. The geometry of these sections are shown in Figures 37, 38, and 39. The outermost points of the upper and lower control arms are connected via a coupling mechanics so that any displacement of the lower arm affect the upper arm as well. The tubes for these sections are smaller than those used in the frame and the profiles of the tubes are listed in Table 19. Where FUCA stands for forward upper control arm, FLCA stands for forward lower control arm, and FPR stands for front pull rod. If there is an "R" in place of the "F", then it is for the rear equivalent. All four of the suspension springs in the car have spring constants of 250 lbf/in.

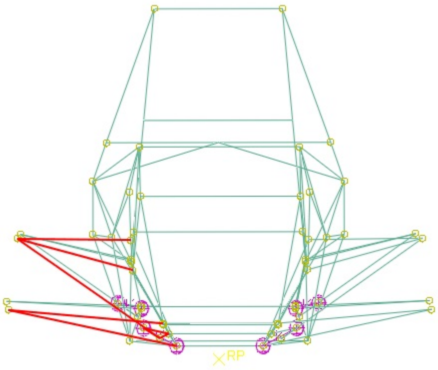

Figure 37: Image with the control arms highlighted from the front.

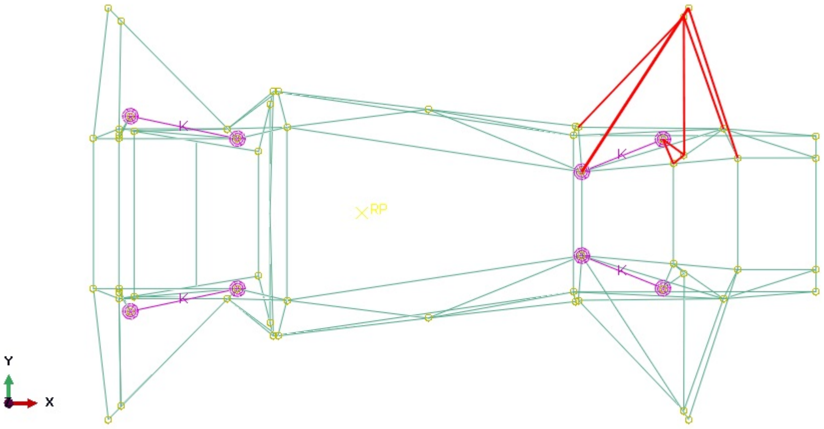

Figure 38: Top view with the front control arms and pull rod highlighted.

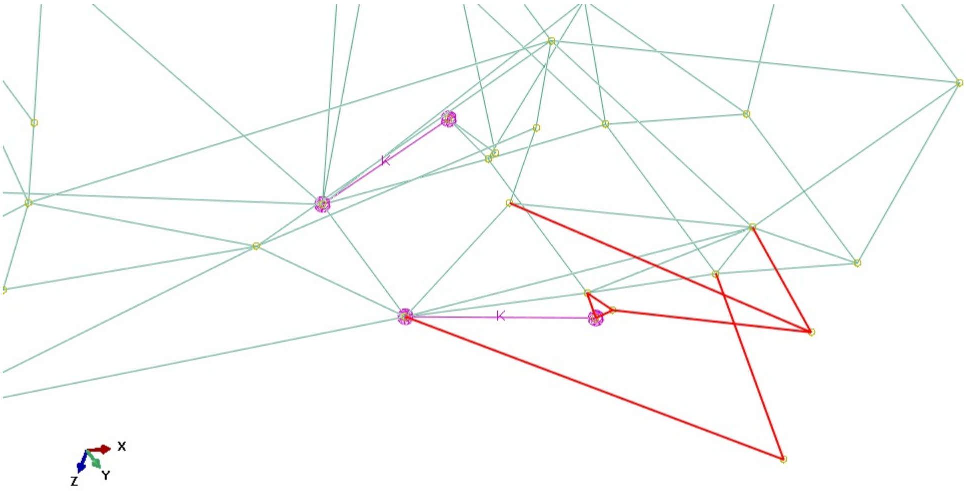

Figure 39: Isometric view with the front control arms and pull rod highlighted. The spring shown is connected to the frame.

Table 19: Upper and lower control arm and pull rod tube profiles.

Member	Outer diameter (in)	Wall thickness (in)
FUCA Aft (MN)	5/8	0.058
FUCA Fore (ML)	1/2	0.035
FLCA Aft (JK)	5/8	0.035
FLCA Fore (JI)	1/2	0.035
FPR (OP)	3/8	0.035
RUCA Aft (BC)	7/16	0.035
RUCA Fore (BA)	7/16	0.035
RLCA Aft (EF)	1/2	0.035
RLCA Fore (ED)	5/8	0.049
RPR (ST)	3/8	0.035

10.3 Natural Frequency and Convergence

The system is set up with free-free boundary conditions to determine the natural frequencies of the chassis. The chassis comprises 132 quadratic beam elements in 3-D space (Abaqus B23 beam elements). Each beam element was meshed with 3 elements along its length to achieve convergence. The resulting first natural frequency for each of these conditions is shown in Table 20. The natural frequency of the first torsional mode shape, using 396 elements is 97.8 Hz, and it converged to ±.03272 percent. This is very good convergence and was used for the steel for the remainder of the simulations. The mode shapes of the first three natural frequencies are shown in Figures 40, 41, and 42, respectively. Each of these images shows a different natural frequency, so the viewer can easily see the major direction of motion. The values at which these natural frequencies were generated on the chassis are shown in Table 21. The first natural frequency is the torsional frequency which exhibits rotation about the longitudinal axis of the chassis. The second is the first lateral bending natural frequency which is shown from a top view, and the third is a transverse bending mode shown from a side view.

Table 20: Natural frequency convergence of the steel frame chassis

Number of elements	First Torsional Natural Frequency (Hz)	% difference
132	98.4	
264	97.8	0.588
396	97.8	0.0327

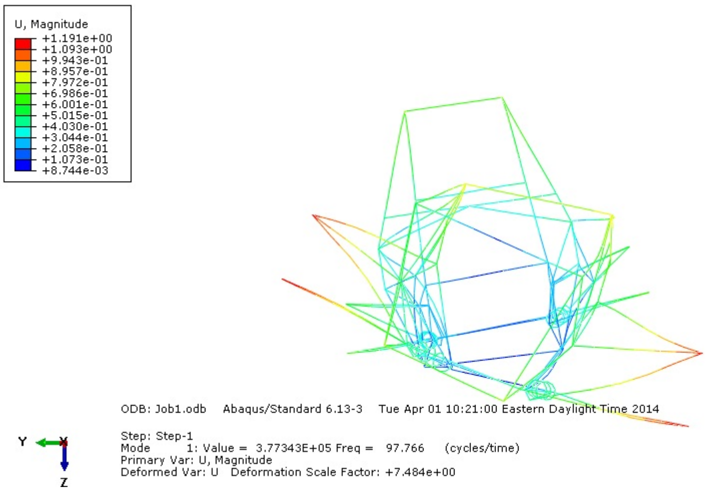

```
ODB: Job1.odb    Abaqus/Standard 6.13-3    Tue Apr 01 10:21:00 Eastern Daylight Time 2014

Step: Step-1
Mode        1: Value =  3.77343E+05 Freq =   97.766     (cycles/time)
Primary Var: U, Magnitude
Deformed Var: U   Deformation Scale Factor: +7.484e+00
```

Figure 40: First torsional natural frequecy. View along the X-direction.

Table 21: First three natural frequencies of the steel frame chassis.

Mode shape	Frequency (Hz)	Percent Difference
Torsion 1	97.766	0.104
Lateral 1	131.11	0.0764
Transverse 1	190.72	0.137

10.4 Simulated Load Cases

The load cases shown in Table 22 have been applied to the steel frame chassis and were compared to the optimized model at the end of this work. The set of load cases was described by Heiβing as a method of preliminary determination of strength and stiffness of a chassis frame. The displacement shown is the maximum displacement of the chassis when pinned at the wheel centers and loaded with accelerations in the directions associated with each load case. The pinned boundary condition scenario is shown in Figure 43.

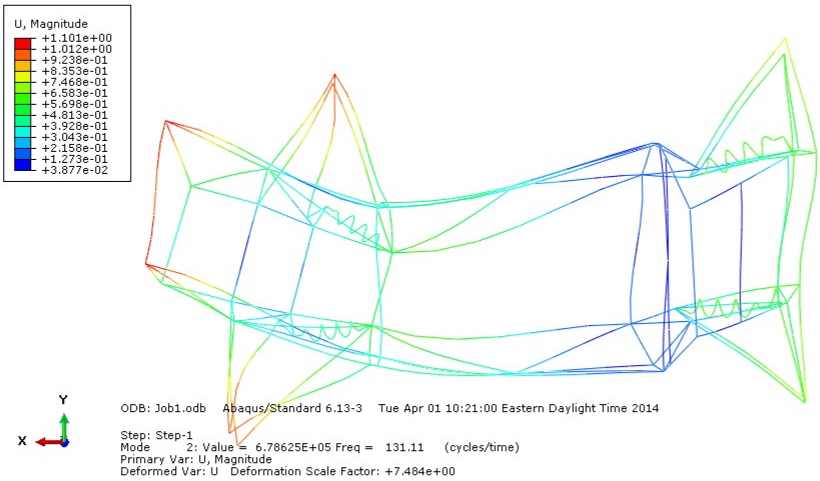

Figure 41: First lateral bending natural frequency. View along the Z-direction.

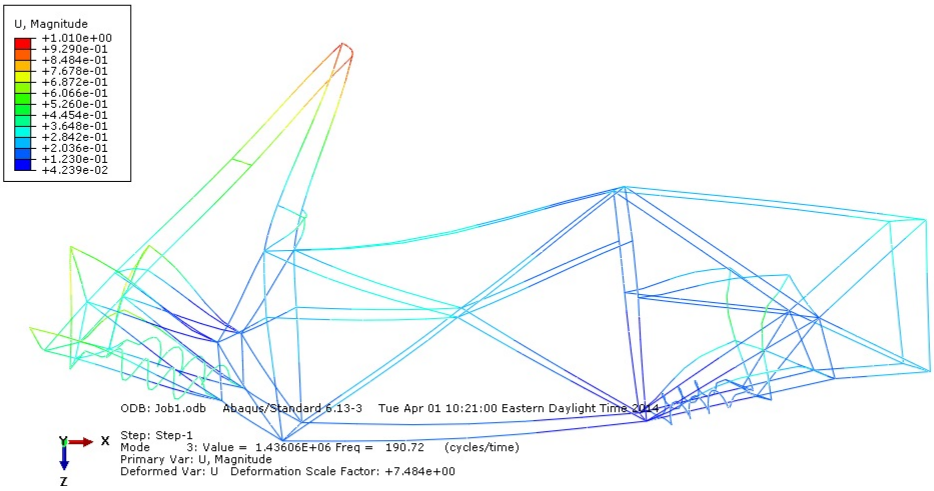

Figure 42: First transverse bending natural frequency. View along the Y-direction.

Table 22: Simulated loading maximum displacements

Load Case	Maximum Displacement (in)
stationary	6.17E-03
vertical bump	1.85E-02
longitudinal bump	1.50E-02
lateral bump	1.40E-02
cornering right	8.81E-03
braking and cornering	9.24E-03
braking in reverse	8.99E-03
acceleration	6.88E-03
acceleration and cornering	6.96E-03

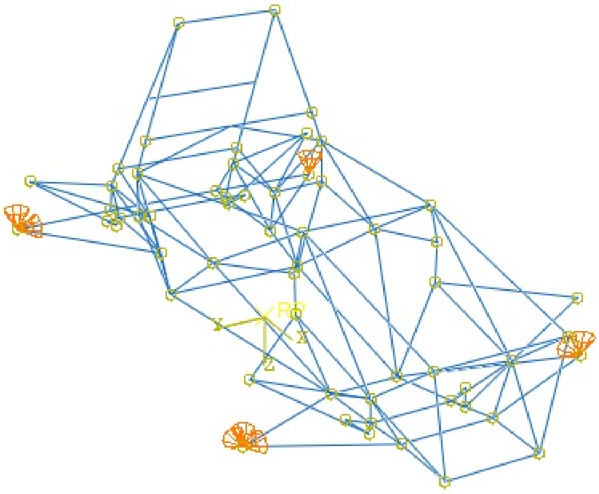

Figure 43: Pinned displacement boundary conditions at the wheel centers for the load cases. The upper control arms are directly connected to the lower control arms.

10.5 Chassis with Composite and Convergence

The chassis was fitted with composite panels on the sides and bottom of the car. The 2014 VT FSAE chassis uses load bearing composite materials on the bottom panel of the chassis as shown in Figure 44. While this is an effective method of enhancing the rigidity of the structure, it does not take full advantage of the structural potential of composite panels because it did not take into consideration tailoring the orientation of the carbon-fiber fabric. A prospective area of improvement is to integrate load bearing composite-side panels on the chassis as shown in Figure 45. The current side panels are not load bearing but provide aerodynamic improvement and close-out the cockpit for some protection for the driver. If the strength-bearing side panels can be activated to shearing, torsional, and bending loads, a more rigid structure can be developed while adding little, if any, weight. Putting the two scenarios together results in both side and bottom panels as shown in Figure 46. The floor and side-panel composite panels are shown as different colors to emphasize that each can have a unique composite layup. For example, the bottom panel could be made with four layers and the side panels with six layers, if that is the design configuration that the optimization process determines to be the best relative to the defined objective function, which maximizes stiffness per unit mass for the torsional, lateral bending and transverse bending cases.

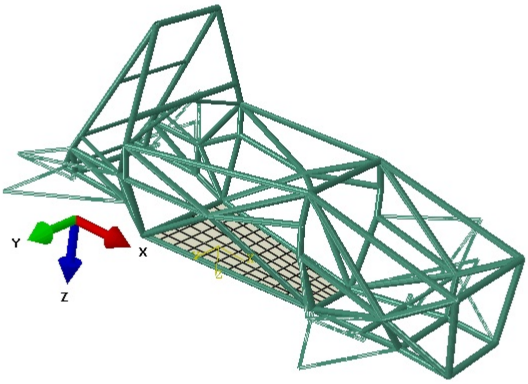

Figure 44: Image of the chassis with just the bottom panel attached.

The composite material properties determined through composite material testing and optimization have been transcribed to Table 23 from section 8.1 of this thesis. The material properties for the

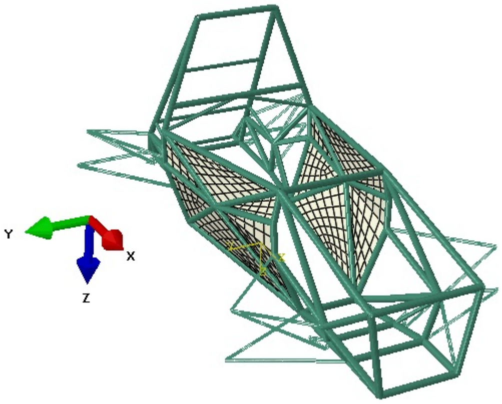

Figure 45: Image of the chassis with just the side panels attached.

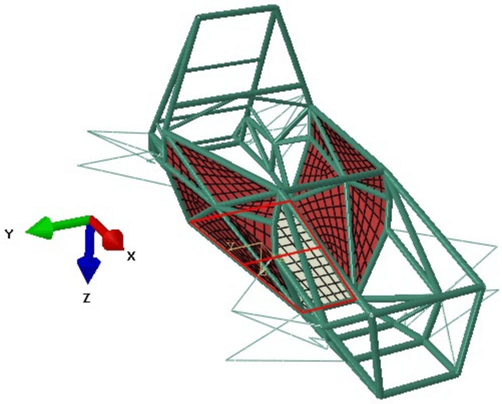

Figure 46: Image of the chassis with both the side and bottom panels attached. The two sections are different colors because the layup may be different in each area.

foam core used are listed in Table 24. Also, the stacking sequences of the composite layups have been tabulated by number of plies in the sequence. It was important to make the stacking sequences balanced and symmetric as shown in Table 25 in order to reduce warping during construction and adverse effects during use. For two layer laminates, a symmetric ply orientation is used instead of a balanced one.

Table 23: Composite material properties

Woven [0/90]s composite	Value	Units
E1	4.52	Mpsi
E2	4.82	Mpsi
ν	.0667	N/A
Lamina Thickness	0.0178475	in
Maximum Strain	0.0108	in/in
Maximum Stress	71.8	ksi

Table 24: Hexcel A1-64-6 Honeycomb Material Properties. Source: Angelini, Nicholas A., 2014, "Simulating Dynamic Vehicle Maneuvers Using Finite Elements for Use in Design of Integrated Composite Structure," Masters Thesis. Virginia Polytechnic Institute and State University, Blacksburg, Virginia.

Property	Value	Units
E1, E2	.1	Kpsi
E3	27.7	Kpsi
$\nu_{1,2}$	.2	N/A
$\nu_{2,3}$,$\nu_{1,3}$	.01	N/A
$G_{1,2}$	4.786	Kpsi
Mass density	6.4e-8	lbf*in/s/s

Table 25: Composite layup stacking sequences by number of plies

Number of Plies	Layup	Example Layup (degrees)
2	[+x/-x]	[20/-20]
4	[+x/-x]s	[20/-20]s
6	[+x/-x/0]s	[20/-20/0]s
8	[+x/-x/+y/-y]s	[20/-20/35/-35]s

11 Half-Scale Chassis Optimization

The half-scale chassis, previously mentioned during the experimental frequency analysis study, is designed so that the natural frequencies match those of the 2013 VT FSAE full-scale car chassis. The geometry of the half-scale is simpler than the full scale, and will be used to demonstrate how the optimization simulation will proceed and to develop the modeling methods. The half-scale chassis has fewer tubes than the full-scale chassis, and all the tubes have the same dimensions as opposed to different dimensions for different tubes. The optimization simulations were conducted in two parts, each part is written to document each phase of the modeling technique used. The first part is optimizing one rectangular panel alone. With simply supported constraints along all the edges, this simplification moderately replicates what each panel experiences, but will not activate the bending moments of the panel. The second part evaluates the full structure with panels affixed to each side and the bottom, and then optimizes the structure. Both parts examined a variety of ply orientations. The effect of the ply number, orientation, and location will be shown; the best laminate configuration will be determined.

11.1 Solitary Panel Optimization

The optimization of the chassis augmented with integrated carbon-fiber panels began by simulating the boundary conditions of a single carbon-fiber panel as a first step towards a solution. It was assumed that the composite panel is attached to the structure with fours sides simply supported. The true boundary condition of the attached composite panel results in a edge stiffness between that associated with the pinned and fixed boundary condition. Whitney [11] shows that a composite simply supported rectangular plate under transverse loads experience maximum deflection according to Equation 27.

$$w_{max} = k\frac{qa^4}{D_{11}} \tag{27}$$

where:
w_{max} = maximum deflection (in)
k = constant determined by solving an integral equation explained Whitney
a = side length of the square plate (in)
D_{11} = First component of the D matrix
q = transverse load (lbf/in^2)

For the purpose of studying the solitary carbon-fiber panel, the constants *k, q,* and *a* do not affect the results because the geometry and loading conditions are the same for every ply layup. The important functional relationship is that the maximum bending displacement is inversely proportional to the D_{11} element of the ABD matrix. Equation 26 can be explored to determine how w_{max} changes over the range of x values with respect to the inverse of the D11 element. A graph of ply orientation with respect to the inverse of the D11 element of the ABD matrix is shown in Figure 47. This graph shows that the maximum deflection for a square panel takes place when the lamina are oriented at ±45 degrees.

A solitary panel with simply supported edges is shown in Figure 48. The solitary composite panel laminates were run through the Matlab code in Appendix E to optimize the first three natural frequencies for each of the composite ply layups. The optimization function is shown in Equation 28. Figure 49 shows the maximum bending and torsional natural frequencies as a function of composite layup. Because the first two potential ply orientations in Figure 49 are a different thickness from the others, the natural frequencies are different; however, for angles thirty to seventy-five degrees of the simulated laminates, the natural frequencies do not vary much, as expected. It would appear the the geometry, the boundary conditions, and the material itself control the natural frequencies rather than the ply orientations. In addition to determining the first bending and torsional natural frequencies, the minimum value of the objective function of Equation 28 is also found. The minimum value of the objective function across the different laminate cases studied is found at an ply orientation value of 40 degree. The actual values are not important as they are not related to the physical chassis structure, only the maximum values.

$$Minimize\,F(x) = F(\theta, \phi, number\,of\,plies) = -(F_{bend1} - (F_{bend2}) - (F_{tors}) \tag{28}$$

$$0\,degrees < \theta, \phi < 90\,degrees \tag{29}$$

$$number\,of\,plies = 2, 4, 6, 8 \tag{30}$$

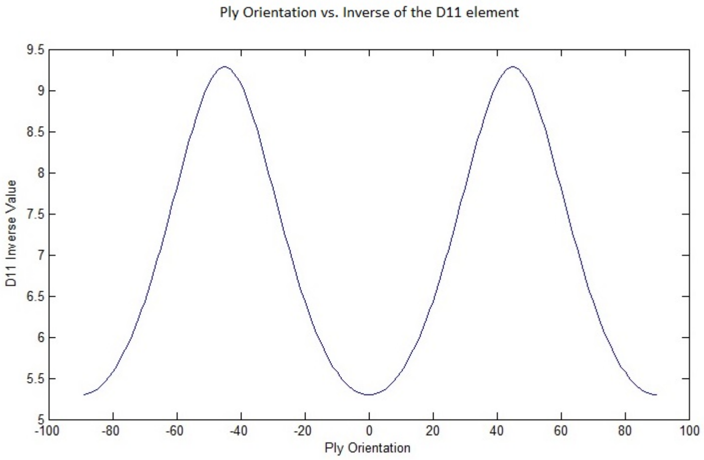

Figure 47: The effect of ply angle on the inverse of the D_{11} element from negative ninety to positive ninety degrees.

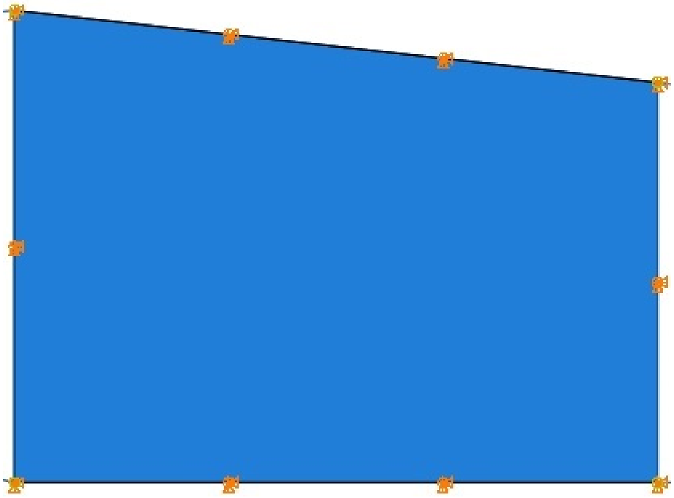

Figure 48: A solitary panel with simply supported edges.

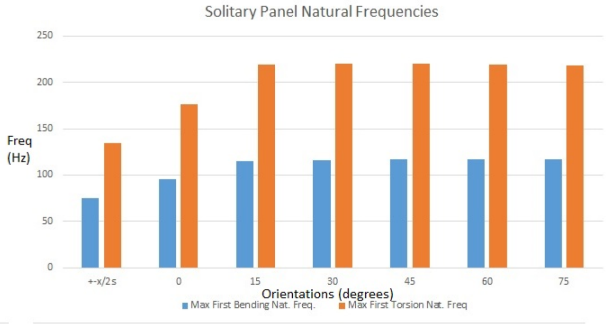

Figure 49: A comparison of the frequency of the maximum first bending and first torsional natural frequencies to each other.

11.2 Combined Panel and Chassis Optimization

In order to determine where the panels will best be utilized, the effect of putting zero-degree plies onto the chassis in three cases: Side Panels Only Case, Bottom Panel Only Case, and Combined Panels Case. The Side Panels Only Case attached plys only to the sides of the chassis. The Bottom Panel Only Case attaches a composite panel to only the bottom of the chassis. The Combined Panels Case attaches panels to both sides and the bottom of of the chassis. The three applications of composite panels to the steel frame are shown in Figures 50, 51, and 52. Convergence shows that as the number of elements in the model increases, the results of the analyses approaches a specific value. The convergence graph in Figure 53 shows that as the number of elements in the panel increases, the first three natural frequencies show a maximum convergence of .304%.

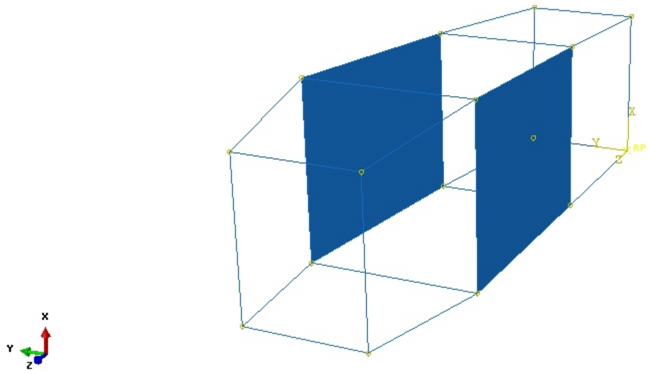

Figure 50: Side Panels Only Case: Side panels attached to the steel frame.

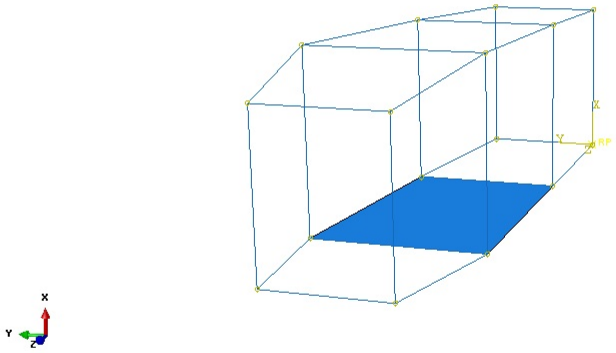

Figure 51: Bottom Panel Only Case: Bottom panel attached to the steel frame.

11.3 Pinned Chassis Natural Frequencies

The half-scale chassis, previously tested as a hanging structure supported at four corners by bungee cords, will be constrained by pinned BC's on the four corners of the rear bulkhead at the wall as shown in Figure 54. The half-scale chassis was tested in Abaqus, and the first and second bending modes as well as the first torsional natural frequency were determined. In the following pictures, the black outlined shape is the original, undeformed geometry of the chassis, and the colored shape is the mode shape of the chassis at the natural frequency. The first bending mode shown in Figure 55 was at 16.94 Hz. The second bending mode shown in Figure 56 occurred at 17.85 Hz. The first torsional mode is shown in

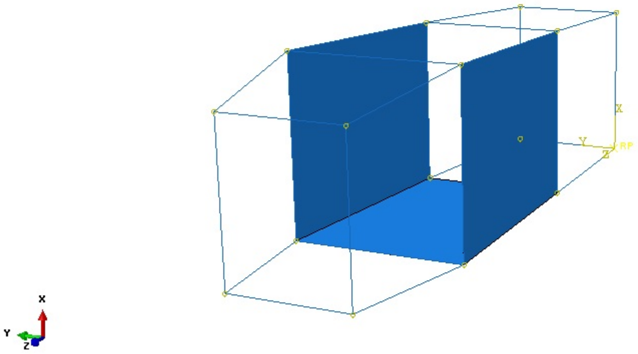

Figure 52: Combined Panels Case: Both side and bottom panels attached to the steel frame.

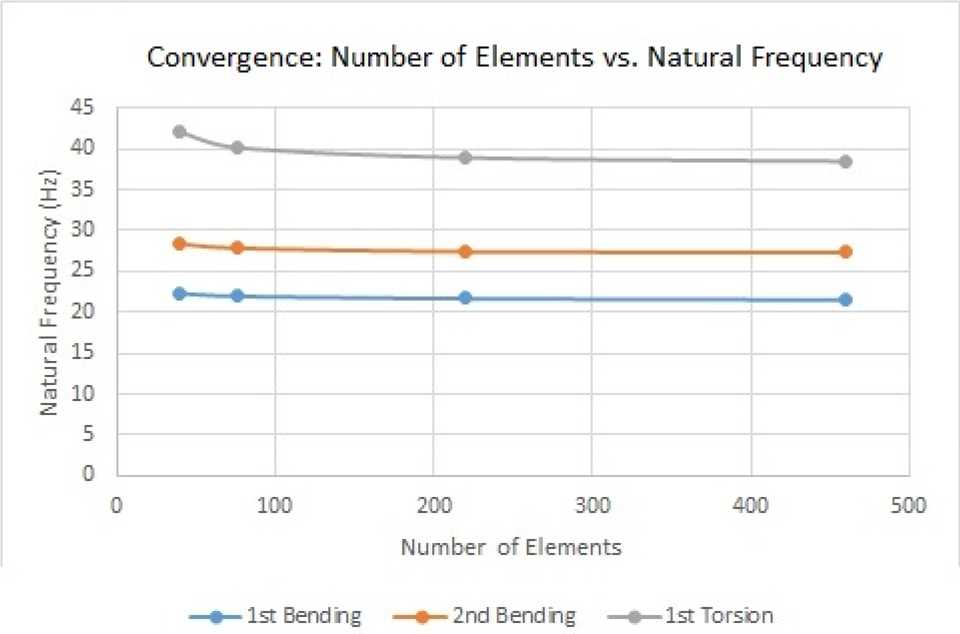

Figure 53: Convergence of the Abaqus model as the number of elements in the model increases.

Figure 57 and occurred at 26.6 Hz. This section focuses upon adding side panels to the structure. The side panels stiffened the chassis; however, the second bending mode and the first torsional mode were impacted by the addition of side panels. The first bending mode was unchanged because side panels prevent transverse bending and torsion, but not lateral bending.

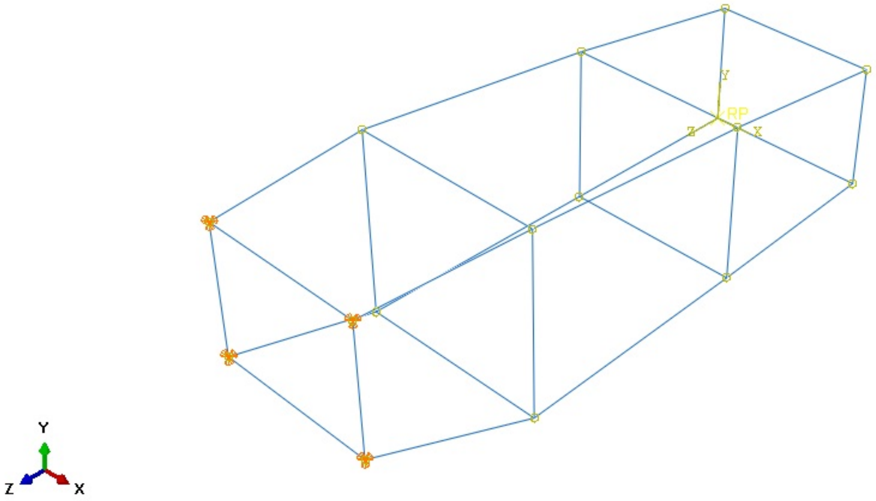

Figure 54: The chassis is constrained by pinned boundary conditions on the four corners of the rear bulkhead.

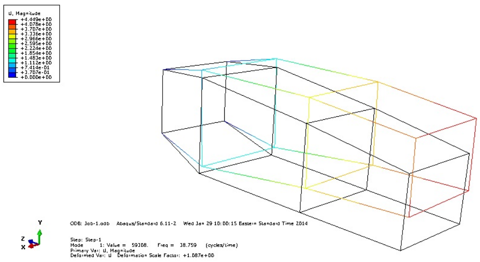

Figure 55: First transverse bending natural frequency of the chassis at 16.94 Hz.

The effect of increasing the number of plies from zero to eight have been documented, and a law of diminishing returns was witnessed for each case. Figure 58 shows how increasing the number of side panel plies affects the second two of the first three structural modes and natural frequencies of the system. The first bending natural frequency of the system is not altered by adding side panels. Figure 59 displays the law of diminishing returns with increasing the number of plies in the bottom of the chassis.

By simply integrating a composite panel on the bottom of the half-scale chassis, the natural frequencies were not increased by a large margin. Figure 60 shows how incorporating plies on the sides and the bottom of the chassis works together to increase all three of the first natural frequencies by up to fifty percent. From this preliminary analysis, one sees a maximum increase of 28.3, 64.9, and 46 percent for the first 3 natural frequencies of the system, respectively. The Side Panels Only case showed a greater than thirty percent increase in the first lateral bending and torsional natural frequencies. The Bottom Only case showed a greater than twenty percent increase for the first lateral bending and first torsional bending of the system. Both the Side Panels Only case and the Bottom Panel Only case only affect the first lateral bending and first torsional mode shapes. The Combined Panels case increase the first lateral bending and first torsional bending by almost eighty percent and the first transverse bending by thirty percent. The ply layup uses eight zero-degree plies on the sides and bottom. A more accurate description of the

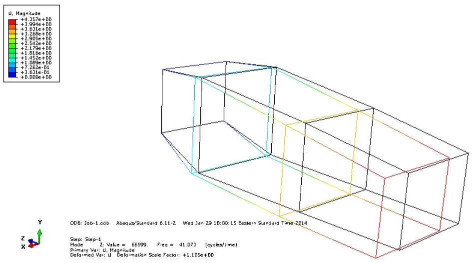

Figure 56: First lateral bending natural frequency at 17.85 Hz.

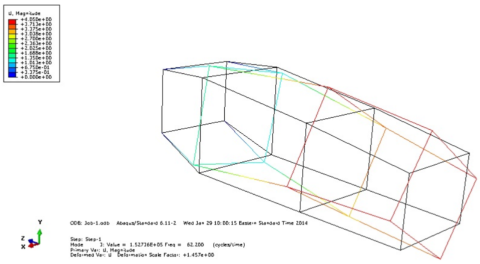

Figure 57: First torsional natural frequency at 26.6 Hz.

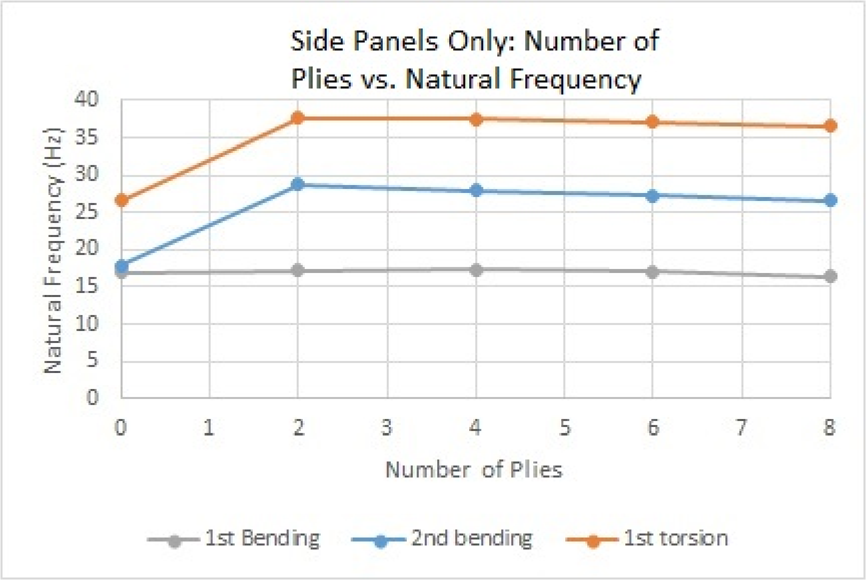

Figure 58: Side Panels Case: Change in natural frequency as number of plies increases.

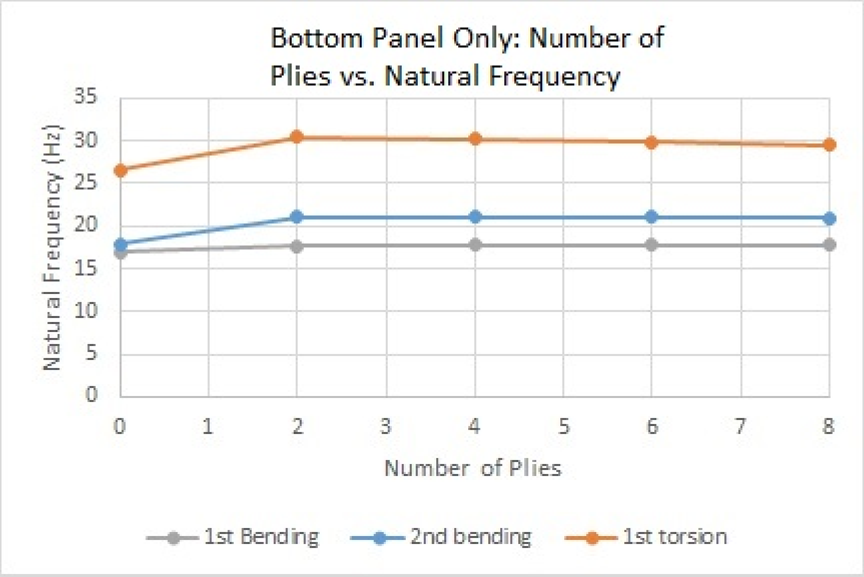

Figure 59: Bottom Panel Case: Change in natural frequency as number of plies increases.

percent advantages gained by adding plies to the bottom, sides, and both are shown in Tables 26, 27 and 28. When the structure is optimized, even higher values are expected.

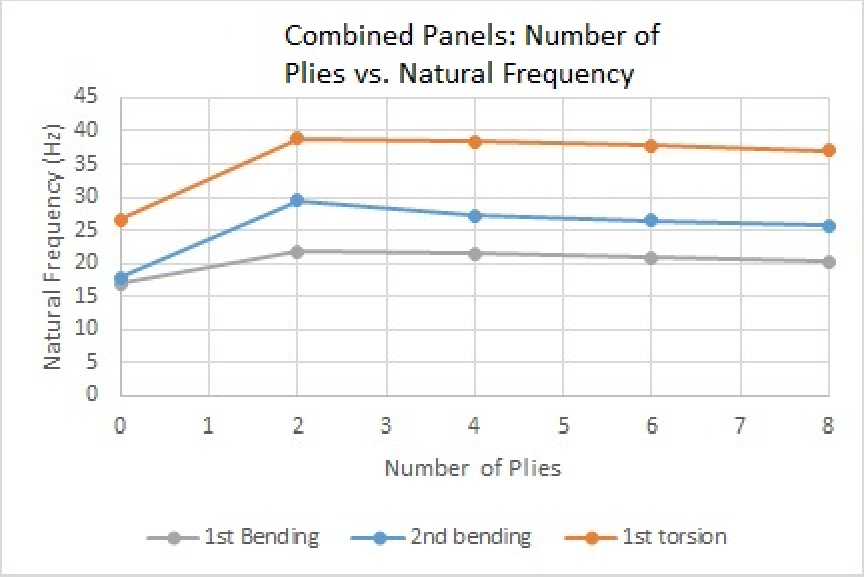

Figure 60: Combined Panel Case: Change in natural frequency as number of plies increases.

11.4 Optimization Comparison

The best setup was determined to utilize both side panels and a bottom panel, this setup was used in determining the optimized ply layup. The first transverse bending, first lateral bending and first torsional modes of the steel chassis have natural frequencies of 16.942, 17.848, and 26.6 Hz, respectively. The optimal orientation varied from 4, 6, and 8 plies as shown in Figure 61. Based on the same optimization function, the optimal orientation is 2 plies at twenty-four degrees followed by 4 plies at forty degrees, 6 plies at thirty-six degrees, and 8 plies at forty-four degrees. By adding more plies at their associated optimal value, the resulting objective function increases in value meaning that the solution is worse than when fewer plies are used. From this half-scale study, it is determined that the Combined Panels Case gives the best results and more plies may not result in better results.

Table 26: Bottom Panel Only Case: natural frequencies

Number of Layers	1st bending (Hz)	2nd bending (Hz)	1st torsion (Hz)
Original Steel Chassis	16.94	17.85	26.6
% diff	0	0	0
2	17.7	21.0	30.5
% diff	4.24	17.9	14.5
4	17.7	21.1	30.2
% diff	4.59	18.2	13.6
6	17.7	21.1	29.9
% diff	4.69	17.98	12.2
8	17.7	21.0	29.5
% diff	4.69	17.59	10.87

Table 27: Side Panels Only Case: natural frequencies

Number of Layers	1st bending (Hz)	2nd bending(Hz)	1st torsion (Hz)
0	16.9	17.9	26.6
% diff	0	0	0
2	17.3	28.7	37.6
% diff	1.96	60.9	41.43
4	17.3	28.0	37.6
% diff	2.054	56.67	41.21
6	17.0	27.2	37.1
% diff	0.602	52.5	39.5
8	16.4	26.6	36.6
% diff	-3.347	48.87	37.497

Table 28: Combined Panels Case: natural frequencies

Number of Layers	1st bending (Hz)	2nd bending (Hz)	1st torsion (Hz)
0	16.9	17.9	26.6
% diff	0	0	0
2	21.8	29.4	38.9
% diff	28.36	64.94	46.39
4	21.5	27.3	38.5
% diff	26.78	52.89	44.67
6	20.9	26.5	37.8
% diff	23.35	48.22	41.90
8	20.3	25.7	37.0
% diff	19.76	44	39.24

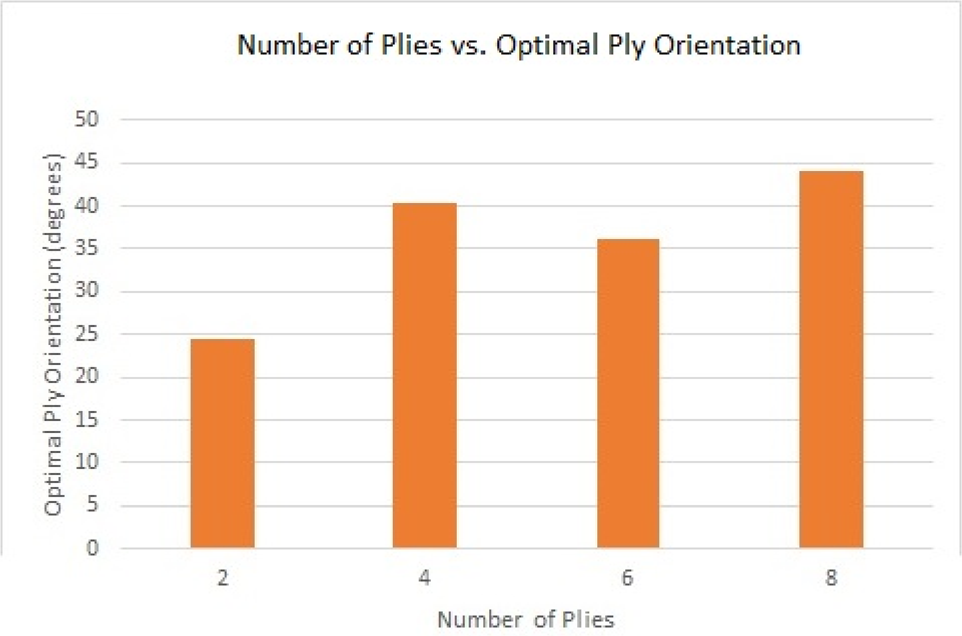

Figure 61: Half-scale: variation of number of plies to the optimal ply orientation.

12 Full-Scale Chassis Optimization

The Abaqus 2013 VT FSAE space frame chassis model augmented with composite panels on the bottom and sides has been optimized relative to the objective function. The best solution for the purpose of this work is defined as one that maximizes the sum of the first three normalized natural frequencies. Several optimized solutions are shown in Table 29, where the lowest objective function values are the best. These solutions are organized by the number of plies on the bottom, the number of plies on the side, and their orientations. In the column "Number of Plies," the number of plies is listed as "AxB", where A is the number of plies on the bottom, and B is the number of plies on the side. The orientations of the plies are listed in the full-scale design section of this report. The best composite panel configuration for eight plies on the bottom and eight plies on the side are -31.7 degrees on the bottom and -89.4 degrees on the sides. While the potential for two different orientations existed for each 8-ply laminate $[\pm\theta/\pm\phi]_S$, the values converged during optimization. The top three solutions are highlighted in gray.

Table 29: Full-Scale Unrounded Optimaztion Results

Number of Plies	Bottom θ 1	Bottom θ 2	Side θ 1	Side θ 2	Objective Function Value	Layup Number
4x2	-72.678	x	-90.356	x	-3.4697	
4x4	-25.9	x	1.8	x	-3.479	
4x6	-25.8842	x	-89.815	x	-3.4854	
4x8	-65.9	x	-86	-0.5	-3.48895	3
6x2	-59.526	x	-89.659	x	-3.47084	
6x4	-65.7	x	-90.6	x	-3.48106	
6x6	-48.8	x	-3.3	x	-3.4862	
6x8	-52.97	x	-87.69	-34.4	-3.48103	
8x2	-24.8	-16.3	-89	x	-3.47149	
8x4	-28.67	-27.97	-89.4	x	-3.48206	
8x6	-53.11	-37.1	-88.48	x	-3.48802	2
8x8	-31.2	-31.7	-88.83	-89.31	-3.49224	1

These values, determined from the optimization code, are not round numbers and it is not feasible to manufacture the carbon fiber on the order of tenths or hundredths of a degree, due to the hand layup manufacturing process. Because of the manufacturing constraints, the orientations have been rounded to the nearest five degrees and recalculated vales are shown in Table 30. The differences as a function of number of plies between the unrounded and rounded results are shown in Figure 62. Using eight plies on both the bottom and sides gives the best results. Figure 62 shows a law of diminishing returns. When using both four and eight plies on the bottom, the point at which more weight than stiffness is added has not yet been reached, but the differences from one bar to the next is decreasing by large amounts. In particular, when six plies are used on the bottom, the optimum value is six on the bottom and six on the side, outranking the use of eight on the side. If we were to increase the number of plies further when using four plies on the bottom, the objective function may flatten or start to increase in value. The total weight of the top three solutions are shown in Table 31.

While the effect of rotating or adding plies can increase or decrease the stiffness of the structure, an investigation was conducted into whether the thickness of the core has any effect on the natural frequencies as identified by the objective function. The thickness of the core of the structure was increased from 0 to .4 inches in an attempt to replicate what may be built into the composite structure on the chassis. The results of the core thickness analysis are shown in Figure 63. As the thickness of the core increases, the natural frequencies of the system increase as well. It agrees with what was expected in that if the composites are moved farther from the bending axis and center of twist, a higher stiffness will result. Based on this analysis, the effect of the core thickness is higher than the effect of optimizing ply orientations. A thicker core results in a higher stiffness per unit mass.

Table 30: Full-Scale Rounded Optimiztion Results

Number of Plies	Bottom θ 1	Bottom θ 2	Side θ 1	Side θ 2	Objective Function Value	Layup number
4x2	-70	-90	x	x	-3.4696	
4x4	-25	0	x	x	-3.479	
4x6	-35	0	x	x	-3.4845	
4x8	-65	x	-85	0	-3.48828	3
6x2	-60	-90	x	x	-3.4707	
6x4	-65	-90	x	x	-3.481	
6x6	-50	-5	x	x	-3.4862	
6x8	-55	x	-90	-35	-3.48103	
8x2	-25	-15	-90	x	-3.47149	
8x4	-30	-30	-90	x	-3.48206	
8x6	-55	-35	-90	x	-3.488	2
8x8	-30	-30	-90	-90	-3.49237	1

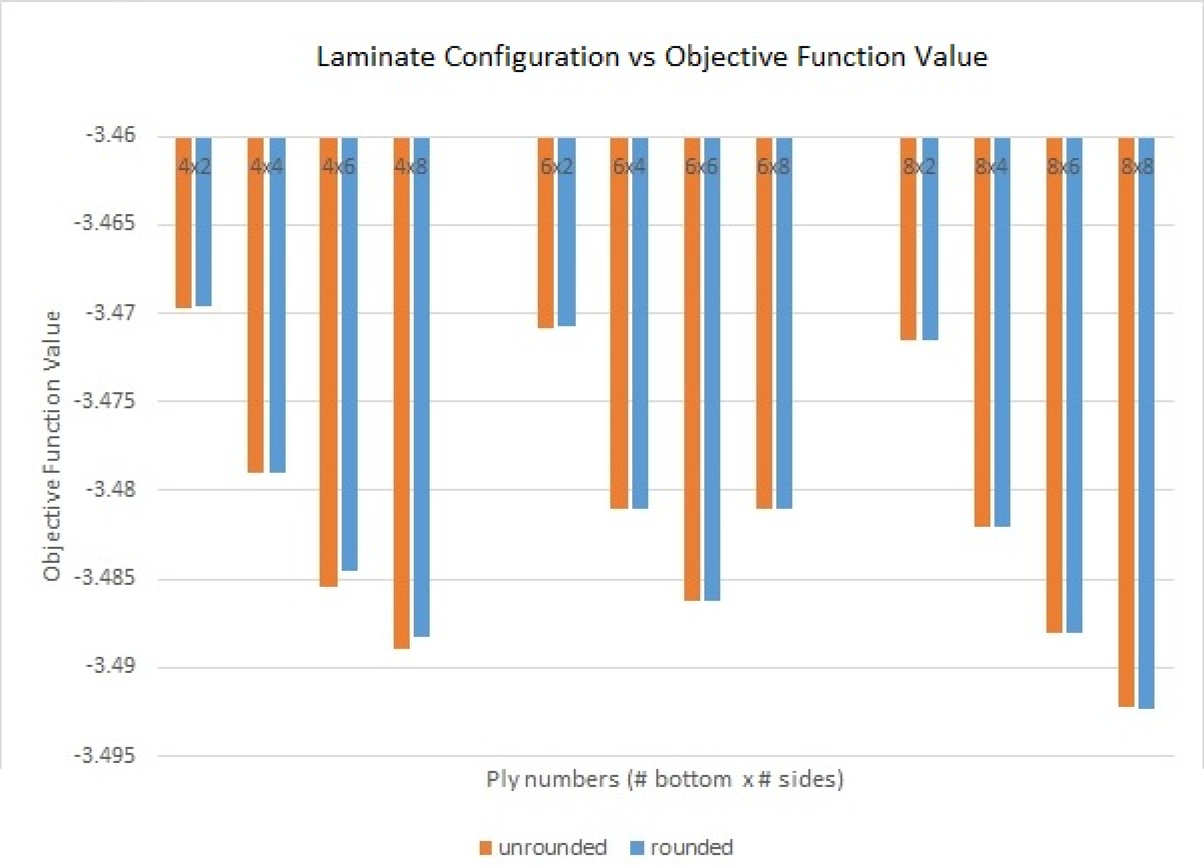

Figure 62: Objective function values for both the unrounded and rounded optimization results.

Table 31: Weight comparison between the steel frame and the top three models.

Model	Weight (lb)
Steel	124
1 8x8	134
2 8x6	133
3 4x8	133

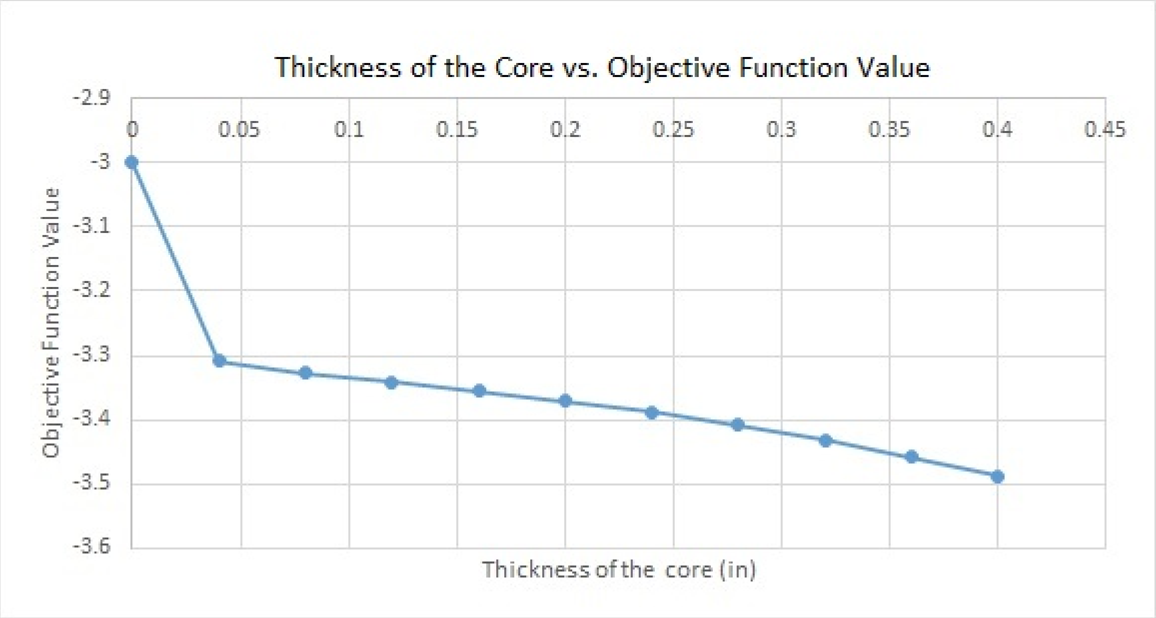

Figure 63: The effect of the increasing the thickness of the core on the objective function.

13 Discussion

This section of the thesis compares the natural frequencies and applied load cases that were analyzed in previous sections. The results are compiled and the differences discussed.

13.1 Natural frequencies

The natural frequencies of the steel VT FSAE space frame chassis and the chassis augmented with carbon-fiber panels on both the bottom and the side of the cockpit have been researched and were discussed in previous sections. The optimized composite laminates were determined using an objective function and the top three laminate configurations are highlighted. Table 32 compares the natural frequencies of the first three modes of the different chassis models. The natural frequencies across the three different composite layups do not change significantly, but they are significantly better than the original steel frame. The first, second and third natural frequencies improved performance by 16%, 26%, and 6% percent respectively. A 16% improvement in the natural frequency of the first torsional mode resulted solely from the inclusion of a thick foam core in the center of the laminate. By moving the two halves of the laminates farther from the bending axis, the stiffness increases significantly.

Table 32: Natural Frequency Comparison: steel vs. three augmented models

Mode shape	Steel (Hz)	8x8 (Hz)	8x6 (Hz)	4x8 (Hz)	Percent increase
Torsion 1	97.8	113.3	113.4	113.6	16
Lateral 1	131	166.3	166.3	166.1	26
Transverse 1	190.7	202.5	202.2	202.5	6

13.2 Load cases

The standard load cases and their resulting displacements were compiled for the steel frame and the three top layups as determined by the optimization code. The results are shown in Table 33. As seen with the natural frequencies, there was very little difference between the three different potential layups. The displacements in all situations decrease by two to three orders of magnitude. Figure 64 shows the differences between the maximum displacements for each of the load cases and laminate configuration. There was only a couple of percent performance difference between each laminate configuration. Because the displacement determined is on the order of 10^{-5}, it would not be practical to see the differences in displacements.

Table 33: Displacements of carbon-fiber panel augmented frame versus only steel frame

Load Case	Steel (in)	8x8 (in)	8x6 (in)	4x8 3 (in)
stationary	6.17E-03	1.71E-05	1.71E-05	1.73E-05
vertical bump	1.85E-02	5.14E-05	5.12E-05	5.20E-05
longitudinal bump	1.50E-02	4.07E-05	4.05E-05	4.10E-05
lateral bump	1.40E-02	3.85E-05	3.80E-05	3.86E-05
cornering right	8.81E-03	2.43E-05	2.41E-05	2.44E-05
braking and cornering	9.24E-03	2.16E-05	2.15E-05	2.18E-05
braking in reverse	8.99E-03	2.46E-05	2.44E-05	2.47E-05
acceleration	6.88E-03	1.90E-05	1.89E-05	1.92E-05
acceleration and cornering	6.96E-03	1.92E-05	1.91E-05	1.94E-05

14 Future Research

One areas of future research that may be investigated to further optimize the system is moving the nodal coordinates of the frame itself to develop a higher stiffness.

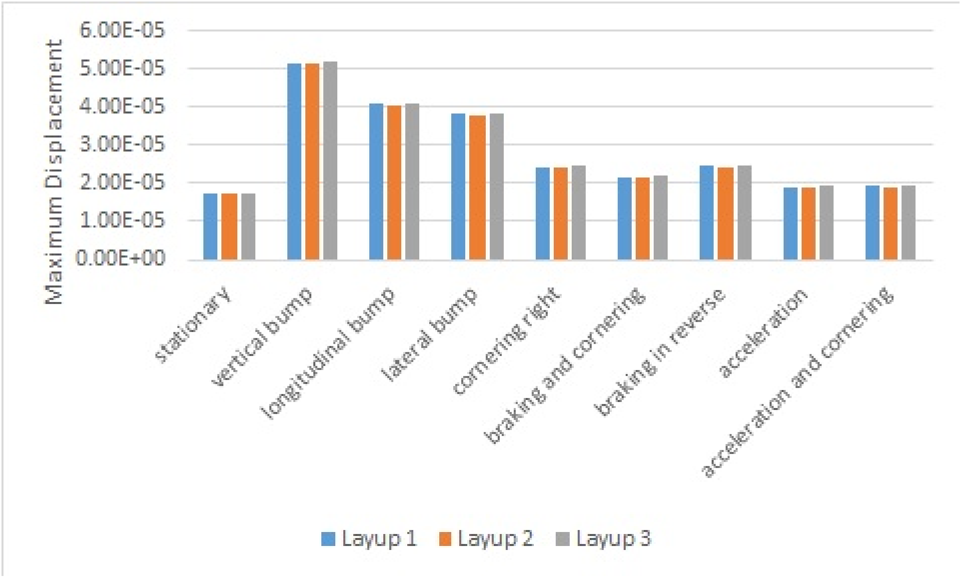

Figure 64: Graph of the different load cases with the three potential layups. The original steel displacement is much greater, and has been left out of this graph for clarity.

14.1 Nodal Positions

In the current research, a few of the nodes are restricted in their potential movement due to subsystem locations (such as the suspension, engine, and race regulations) [4]. The same optimization program that determines the ideal material properties and the ideal ply orientations can also determine the optimal nodal positions. Optimizing nodal positions has been completed in two different ways: Sequential Nodal Movement, Parallel Modal Movement. The initial and final natural frequencies and results of the Sequential Nodal Movement have been shown in Figure 65 and Table 34, where three nodes were moved one after the other. The results of Parallel Nodal Movement are shown in Figure 66 where two nodes were moved simultaneously. The final position of the connecting node in Figure 66 is not optimized because it appears to be misaligned. The nodes can be adjusted in later steps or through the addition of constraint equations to the nonlinear programming model. Optimizing chassis node placement can be pursued immediately with results that increase the first three natural frequencies 8.55, 18.5 and 4.86 %, respectively.

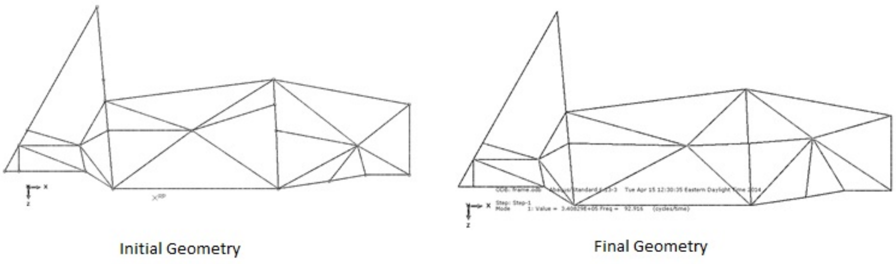

Figure 65: Initial and final geometry of the side of the chassis optimizing three nodes in series.

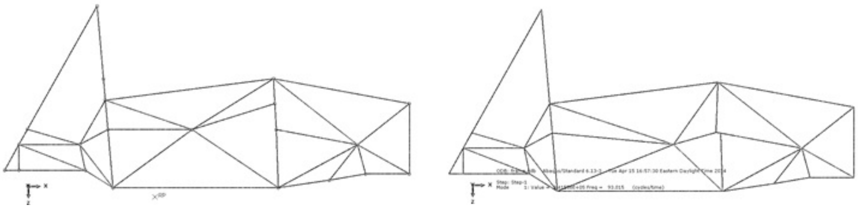

Figure 66: Initial and final geometry of the side of the chassis optimizing two points simultaneously

Table 34: Initial and final natural frequencies following node position optimization.

Model	T1 (Hz)	B1 (Hz)	B2 (Hz)
Initial	97.8	131.1	190.7
Sequential Nodal Movement	105.9	158.9	199.4
Parallel Nodal Movement	106.1	155.4	199.9
Percent difference between the Steel Chassis and Parallel Nodal Movement	8.55	18.504	4.86

15 Conclusion

The purpose of this work was to use finite element analysis to optimize ply orientation and stacking sequence of carbon-fiber panels added to the space frame Formula SAE chassis. Carbon-fiber panel optimization involved measuring the tensile composite material properties, a prototype was analyzed, and the full-scale chassis was optimized using computer analysis. An optimization problem was formulated as a non-linear problem, and the optimal composite panels were determined. The laminate configuration that maximized the natural frequencies used eight ±30 degree plies on the bottom and eight ±90 degree plies on the sides of the chassis.

Composite Test Composite materials used in the simulation had the same material properties as the physical versions used for testing. The E_1, E_2, and ν_{12} properties were initially determined by testing coupons of the materials in tension on the Instron load frame in Randolph Hall at Virginia Tech. The machine was first checked for alignment and was found to be aligned along the long axis, and slightly out of alignment in the wide axis. The ten-inch long composite specimens were tabbed using deadsoft aluminum and a 100x100 stainless steel mesh. In addition, strain gages were affixed to the specimens to calculate strain more accurately. From 11 total samples measured at zero, ninety, and forty-five degrees, a set of preliminary composite material property data was gathered.

An Abaqus model of a 10x1 inch specimen was developed to conform with the properties found through laboratory testing. The stress-strain results from this model were compared to several data sets from the test and were found to have a systemic error that would result in an exaggerated stress for every strain. Because of the error, the material properties and the simulated specimen were input into an optimization code to determine the true Young's modulus in the 1- and 2-directions. When the error over the entire strain gage range was minimized, the Young's modulus in the 1-direction decreased by .29 percent and the Young's modulus in the 2-direction increased by 3.14 percent. Once the material properties were determined, the analysis and optimization of the half-scale and full-scale chassis were conducted.

Half-Scale Chassis The purpose of this section was to develop a computer model of a steel chassis constructed of welded tubes, and verify the model with experimental testing of the mode shapes. The frame was tested experimentally and the natural frequencies were identified. The simulation subsection showed the simulation, the resulting mode shapes, and corresponding natural frequencies. The natural frequencies were compared and found to be within 5% for the range from zero to one-hundred fifty Hz. Some extra mode shapes were found experimentally that were not found with the simulation potentially because of coupling with the suspended shaker or the direction of the applied force was incorrect. The mode shapes were compared with the frequency response function determined experimentally along with the corresponding phase angles. The differences in frequency values may be due to the use of nominal geometry of the half-scale chassis in simulation. In addition, the simulated half-scale chassis assumes perfectly bonded joints with beams whose profiles do not vary.

The simulated half-scale chassis was augmented with composite panels. Bottom and side panels were added individually and together to measure different possible configurations. The addition of side and bottom panels together resulted in the highest natural frequencies, increasing the first, second and third natural frequencies (54, 85, and 91 Hz, respectively) by 20, 44, and 40 percent, respectively. The optimum number of plies for the half-scale chassis is two when the bottom and sides are used together. This result was unexpected as it would appear that adding more would increase the stiffness. However, due to the low mass of the system, the addition of 8 plies per panel increased the mass without increasing the stiffness a proportional amount, resulting in lower natural frequencies. It is important to raise the natural frequencies of the chassis system so that the structure supported by the suspension appears as close to rigid as possible from the perspective of the suspension.

MATLAB Code A MATLAB non-linear optimization model was developed to take inputs of laminate stacking sequence and write the data to the Abaqus input file. The input file is run using MATLAB and the resulting natural frequencies are determined. By using the built-in optimization function in conjunction with the Abaqus code, an optimal value of ply orientation was determined. The objective function is used to determine the performance of the laminate. In this case, the objective function is the negative of the sum of the first three composite natural frequencies normalized to the frequency of the same mode shape of the original space frame chassis.

Full-Scale Optimization The design of the full-scale vehicle has already been set by the 2014 team; however, the orientation of the composite laminates has not been chosen yet. A chassis space frame model was built in Abaqus and the model has been converged to .032% for the first natural frequency. The first three natural frequencies associated with the first lateral bending, first transverse bending and first torsional modes are determined to be 97.8 Hz, 131.1 Hz, and 190.7 Hz, respectively. Composite panels are added to both the bottom and the sides of the structure, as this configuration was determined to result in the highest natural frequencies from the half-scale chassis analysis.

The optimization of the full-scale chassis model is slightly more in-depth than the half scale chassis model, as the side and bottom panels are allowed to comprise different numbers of layers so that any possible combination of two, four, six and eight are available. From practical analysis of the structure, however, any less than 4 plies on the bottom will result in failure due to the driver's weight. The analysis showed that the top three results were 4x8, 8x6, and 8x8 with 8x8 being the top performer. The first number is the number of plies of the bottom panel and the second is the number of plies on the side panel. The 4x8 has less plies then the 8x6, weighs less then the 8x6 which may explain its higher performance. It was found that the optimum orientation for the bottom panel is 30 degrees, and for the side panels is 0 degrees. It is important to note that while there was an increase in strength due to the orientation of the fibers, a larger increase resulted from changing the core thickness. An increase in foam core thickness of .4 inches allows the two halves of the composite structure to be farther from the bending axes. Combining these two effects results in a 16 percent increase in the natural frequency of the first lateral bending mode of the system.

Finite element multi-level analysis can be used to optimize the configurations of carbon-fiber laminates for use in high performance vehicles. The results showed that using the 8 panels on the side at ±90 degrees and 8 panels on the bottom at ±30 degrees resulted in the natural frequencies of the first lateral bending, first transverse bending and first torsional modes of the system increasing by 16, 26 and 6 percent. However, the 4x8 panel configuration resulted in only a 0.15 percent objective function reduction with a one pound weight savings. Greater performance as measured by natural frequency may be achieved by orienting the panels at ±30 degrees and incorporating a honey combed core thickness of .4 inches. It is interesting that adding the core had such a large impact. The effect of the ratio of core material to carbon-fiber in various locations of the body should be investigated. Further analysis should be conducted with a stiffness goal using weight as an optimization function to reduce the mass inertia. This research demonstrates the potential for using finite element multi-level optimization analysis to maximize vehicle natural frequencies. Refinements and improvements in the model need to be validated against stiffness tests of the chassis to provide continued improvement in product design.

References

[1] Abaqus Version 6.13, 2013, 'Abaqus Analysis User's Manual', Dassault Systmes, Providence, RI, USA.

[2] ASTM Standard D3039/D3039M-08, 2013, "Standard Test Method for Tensile Properties of Polymer Matrix Composite Materials," ASTM International, West Conshohocken, PA, 2013, DOI: 10.1520/D3039-D3039M-08, www.astm.org.

[3] United States, Department of Defense, 2002, Composite Materials Handbook, Volume 3 Polymer Matrix Composites, Material Usage, Design and Analysis, Vol. 3, Fort Washington, PA: Materials Science Corporation. Print. MIL-HDBK-17-3F.

[4] "Rules and Important Documents," 2014, Formula SAE, SAE International.

[5] Cook, Robert Davis., David S. Malkus, Michael E. Plesha, and Robert J. Witt, 2002, "Concepts and Applications of Finite Element Analysis," 4th ed., New York: Wiley.

[6] Chen, Wei, Wei Fu, S. B. Biggers, and Robert A. Latour, 2000, "An Affordable Approach for Robust Design of Thick Laminated Composite Structure," Optimization and Engineering 1.3: 305-22.

[7] Haftka, Raphael T., Zafer Gurdal, and Manohar P. Kamat,1990, Elements of Structural Optimization. 2nd ed. Dordrecht: Kluwer Academic.

[8] Bruyneel, M., 2006, "A General and Effective Approach for the Optimal Design of Fiber Reinforced Composite Structures," Composites Science and Technology 66: 1303-314. Science Direct.

[9] Walker, Mark, and Ryan Smith, 2003, "A Methodology to Design Fiber Reinforced Composite Structure for Maximum Strength," Composites Part B: Engineering 34: 209-14. Science Direct.

[10] Karaolis, N.M., Mussgrove, P.J, and Jeronimidis, G, 1988 Active and Passive Aeroelastic Power Control using Asymmetric Fiber Reinforced Laminates for Wind Turbine Blades, Proc. 10th British Wind Energy Conf., D.J. Milbrow Ed., London, March 22-24.

[11] Whitney, James M., 1987, Structural Analysis of Laminated Anisotropic Plates, Lancaster, PA: Technomic.

[12] Genta, Giancarlo, and Lorenzo Morello, 2009, The Automotive Chassis, Berlin: Springer Netherland.

[13] Heldt, P.M., 1945, The Automotive Chassis. (without Powerplant), 1st ed., Nyack, N.Y.

[14] Inman, Daniel J., 2008, Engineering Vibration, 3rd ed., Upper Saddle River, NJ: Pearson Prentice Hall.

[15] Biancolini, M.E., Cerulla, A., and Reccia, L., 2007, "Design of a tuned sandwich chassis for competition go-kart," Int. J. Vehicle Design, Vol. 44, No. 3 and 4, pp. 360-378.

[16] Cristello, Nick, and Il Yong Kim, 2007, "Multidisciplinary Design Optimization of a Zero-emission Vehicle Chassis considering Crashworthiness and Hydroformability," Proceedings of the Institution of Mechanical Engineers, Part D: Journal of Automotive Engineering: DOI: 10.1243/09544070JAUTO440.

[17] Biancolini, M.E., Renzi, F., and Rizzoni, G, 2007, "Design of a lightweight chassis for the land speed record vehicle Buckeye Bullet 2," Int. J. Vehicle Design, Vol. 44, No. 3 and 4, pp. 379-402.

[18] Feraboli, Paolo, and Attilio Masini, 2006, "Development of Carbon/epoxy Structural Components for a High Performance Vehicle," Composites Part B: Engineering 35.4: 323-30, Science Direct.

[19] Masini A, Bonfatti A, and Feraboli P., 2006 "Carbon fiber composites for improved performance of the Murcielago Roadster," In:6th Annual SPE Automotive Composites Conference, Troy, Michigan,

Society of Plastics Engineers

[20] Cavazzuti, Marco, Andrea Baldini, Enrico Bertocchi, Dario Costi, Enrico Torricelli, and Patrizio Moruzzi, 2010, "High Performance Automotive Chassis Design: A Topology Optimization Based Approach," Structural and Multidisciplinary Optimization 44.1.

[21] Angelini, Nicholas A., 2014, "Simulating Dynamic Vehicle Maneuvers Using Finite Elements for Use in Design of Integrated Composite Structure," Masters Thesis. Virginia Polytechnic Institute and State University, Blacksburg, Virginia.

[22] Heiβing, Bernd, and Metin Ersoy, 2011, Chassis Handbook Fundamentals, Driving Dynamics, Components, Mechatronics, Perspectives, Wiesbaden: Vieweg Teubner.

[23] Hyer, M. W., and S. R. White, 2009, Stress Analysis of Fiber-reinforced Composite Materials, Lancaster, PA: DEStech Publications.

[24] Jones, Robert M., 1999, Mechanics of Composite Materials. Philadelphia, PA: Taylor and Francis.

[25] "Vehicle Dynamics Terminology," 1976, J670: Vehicle Dynamics Terminology. Society of Automotive Engineers.

[26] "PCB Model 352C68," PCB Model 352C68, PCB Piezotronics.

[27] "Ling V203 Permanent Magnet Shaker," LDS Model V203, Ling Dynamics Systems.

[28] "PCB Model 288D01," PCB Model 288D01, PCB Piezotronics.

Appendix A: Geometry and Material Properties of the Half-Scale System

Table 35 describes the nodes of the system by coordinates. 60 inch bungee cords are attached to 2 corners on both ends to suspend the structure.

Table 35: Chassis Node Coordinates

Table 1: Chassis Node Coordinates

Vertex	X-coord	Y-coord	Z-coord
	in.	in.	in.
Front Bulkhead			
1	48	6.5	5
2	48	6.5	-5
3	48	-6.5	-5
4	48	-6.5	5
Front Roll Hoop			
5	32	7	6
6	32	7	-6
7	32	-7	-6
8	32	-7	6
Main Roll Hoop			
9	12	7.5	7
10	12	7.5	-7
11	12	-7.5	-7
12	12	-7.5	7
Rear Bulkhead			
13	0	6.5	5
14	0	6.5	-5
15	0	-6.5	-5
16	0	-6.5	5

Table 36: Section Geometry

Section Geometry

Profile	Radius	Thickness
Name	in.	in.
Tube_625_035	0.3125	0.035

Table 37: Material Properties

Material Properties

Material	Elastic Modulus	Shear Modulus	Poisson's Ratio	Weight Density	Yield Strength	Ultimate Strength
	Mpsi	Mpsi		lbf/in3	kpsi	kpsi
Steel 4130 Normalized	29.7	11.6	0.29	2.84	63.1	97.2

Appendix B: Accelerometer, Shaker and Impedence Head Pertinent Properties

Table 38: PCB Piezotronics accelerometer model 352C68. Source: "PCB Model 352C68," PCB Model 352C68, PCB Piezotronics.

Property	English	Si
Sensitivity (10 percent)	10 mV/g	1.02 mV/(m/s)
Measurement Range	±500 g pk	±4900 m/s pk
Frequency Range (5 percent)	0.5 to 10000 Hz	0.5 to 10000 Hz
Frequency Range (10 percent)	0.3 to 15000 Hz	0.3 to 15000 Hz

Table 39: Ling Dynamics Systems Permanent Magnet Shaker V203. Source: "Ling V203 Permanent Magnet Shaker," LDS Model V203, Ling Dynamics Systems.

Sine force, peak	17.8 N
Maximum Sine force peak	26.7 N
Armature Resonance Frequency	13000 Hz
Useful Frequency Range	5 - 13000 Hz
Effective Mass of Moving Element	0.020 kg
Velocity Sine Peak	1.49 m/s
Maximum Velocity Sine Peak	1.83 m/s
Amplifier rating	0.048 kVA
LDS Amplifier	PA25E
Vibrator mass (base)	1.81 kg
Height (base)	96 mm
Width (base)	78 mm diameter

Table 40: PCB Piezotronics Mechanical Impedence Sensor Model 288D01. Source: "PCB Model 288D01," PCB Model 288D01, PCB Piezotronics.

Sensitivity(± 10 %)(Acceleration)	100 mV/g
Sensitivity(± 10 %)(Force)	100 mV/lb
Measurement Range(Acceleration)	± 50 g pk
Measurement Range(Force)	± 50 lbf pk
Frequency Range(: ± 5 %)(Acceleration)	1 to 5000 Hz
Frequency Range(± 10 %)(Acceleration)	.7 to 7000 Hz
Size (Hex x Height)	11/16 in x 0.820 in
Weight	0.68 oz

Appendix C: Space Frame Material and Design Properties

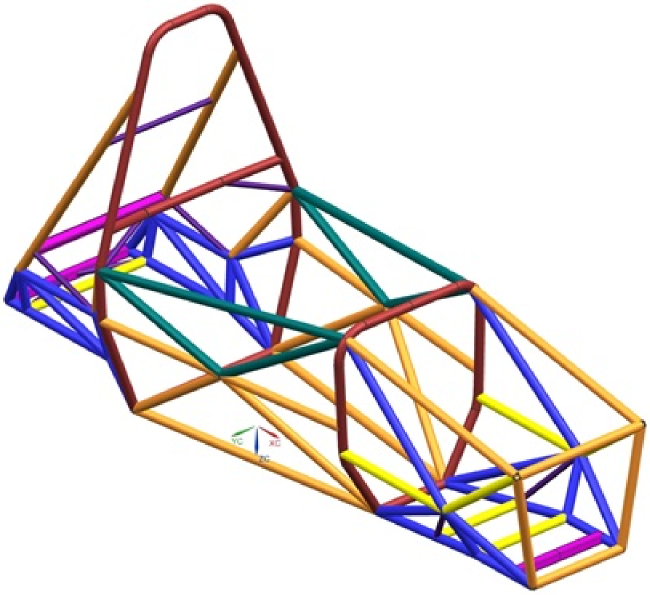

Figure 67: This image shows the different tubes which make up the chassis according to the following table.

Table 41: Tube dimensions associated to the color in the Figure.

Maroon = 1” x 0.095”
Orange = 1” x 0.065”
Blue= 1” x 0.049”
Yellow = 1”x 0.035”
Teal = 1” x 0.028”
Pink = 1” x 1” x 0.035” square tube
Purple = 5/8” x 0.035”

Table 42: Material properties of the steel in the space frame.

Material Spreadsheet Code	**Steel**
Material name	Steel
Youngs Modulus, E	2.00E+11
Yield strength, Pa	3.05E+08
UTS, Pa	3.65E+08
Yield strength, welded, Pa	1.80E+08
UTS welded, Pa	3.00E+08
UTS shear, Pa	2.19E+08

Appendix D: Specimen Geometry

Table 43: Geometric Properties of Each Tested Specimen: Width

	half	quarter1	quarter2	third1	third2	
Specimen	Width 1	Width 2	Width 3	Width 4	Width 5	Width Avg
0-1	0.995	0.977	1.011	0.979	0.996	0.9916
0-2	1.025	1.03	1.021	1.018	1.031	1.025
0-3	1.012	1.002	0.998	1.001	0.991	1.0008
0-4	0.975	0.989	0.977	0.985	0.98	0.9812
90-2	0.995	1.012	1.002	1.013	1.004	1.0052
90-3	1.004	1.01	1.005	1	1.008	1.0054
90-4	1.018	1.009	1.011	1.011	1.011	1.012
45-2	0.989	1.017	0.982	1.008	0.995	0.9982
45-3	1.009	1.002	1.02	0.998	1.016	1.009
45-4	1.006	0.978	1.012	0.978	1.035	1.0018

Table 44: Geometric Properties of Each Tested Specimen: Thickness and Length

	half	quarter1	quarter2	third1	third2		
Specimen	Thick 1	Thick 2	Thick 3	Thick 4	Thick 5	Thick Avg	Length
0-1	0.15	0.145	0.139	0.144	0.146	0.1448	10.022
0-2	0.143	0.145	0.143	0.143	0.139	0.1426	10.003
0-3	0.139	0.14	0.144	0.14	0.144	0.1414	10.055
0-4	0.143	0.133	0.14	0.138	0.137	0.1382	9.939
90-2	0.138	0.14	0.132	0.144	0.143	0.1394	10.018
90-3	0.14	0.143	0.14	0.139	0.14	0.1404	10.003
90-4	0.138	0.134	0.141	0.135	0.137	0.137	9.998
45-2	0.141	0.15	0.149	0.149	0.145	0.1468	10.01
45-3	0.149	0.152	0.15	0.151	0.149	0.1502	9.988
45-4	0.146	0.148	0.15	0.145	0.146	0.147	10

Appendix E: Optimization MATLAB Code

```
clear
clc

N=3;
xmin=[0;0];
fvalmin=1e6;
for i=1:N;
    a=-90+rand(1)*180;
    b=-a;
    c=-90+rand(1)*180;
    d=-c;
    x=[a;c];
    f = myfun(x)
    if f<fvalmin
        fvalmin = f; %if the new function value is
          lower,reset the minimum function value
        xmin=x; %if the new function value is lower
          associate it with the correct a and b values
    end
    fvalmin
end

InitialL1 = xmin(1,1)
InitialL3 = xmin(2,1)

[x,fval,exitflag,output]=GetOrientations(InitialL1,InitialL3)
```

Get Ply Orientation Angles Functions

```
function [x,fval,exitflag,output]=GetOrientations(InitialA,InitialF)
[x,fval,exitflag,output] = Optimize(InitialA,InitialF);
```

Run Minimization Code

```
function [x,fval,exitflag,output] = Optimize(InitialL1,InitialL3)
x0=[InitialL1;InitialL3];
lb = [-90;-90];
ub = [90;90];
options = optimset('TolFun',1e-4,'PlotFcns',@optimplotfval,
  'Algorithm','interior-point');
%[x,fval,exitflag,output]=fminsearch(@myfun,x0,options)
[x,fval,exitflag,output]=fmincon(@myfun,x0,[],[],[],[],lb,ub,[],options)
```

@myfun

```
function f = myfun(x)
pause on
sprintf('starting new job')
% Edit below
NewINP=WriteNewInputFile(x);
% Edit above
JOBName='ChassisTest';
sprintf('evaluating job')
eval(['!abaqus job=',JOBName,' input=',NewINP])
sprintf('job evaluated')
pause(10)
```

```
checkpoint=2;
while checkpoint>0
    gate=exist('ChassisTest.lck','file');
    checkpoint=gate;
    if checkpoint==2
    elseif checkpoint==0
    end
end
sprintf('running script')
AbaqusData=RunScript();
% Edit below
% AbaqusDataStress=ComputeVonMisesSS(AbaqusDataLoad,
  %SpecimenHeight%,%ShearArea%,%YieldExtension%);
% % Edit above
% data1=load('ExactDataLoad');
% Exp1=data1.ExactDataLoad;
% data2=load('ExactDataStress');
% Exp2=data2.ExactDataStress;
% ResultDataLoad=InterpolateData2(AbaqusDataLoad,Exp1);
% ResultDataStress=InterpolateData2(AbaqusDataStress,Exp2);
% save('ResultDataLoad.mat','ResultDataLoad');
% save('ResultDataStress.mat','ResultDataStress');
f=AbaqusData(1,3)
```

Write New Abaqus Input File

```
%Reads an input file into an array of strings, change a specified string,
%output to a new file
function NewINP=WriteNewInputFile(x)
x
%load ExactData.mat;
NewINP=textread('optimize.inp','%s','delimiter','\n');
TestCount=1;
CurrentFile=NewINP;
% Edit below
a5=CurrentFile{1135};
a6=CurrentFile{1136};
a7=CurrentFile{1137};
a8=CurrentFile{1138};
% Edit above
New01=x(1);
New02=-x(1);
New03=x(2);
New04=-x(2);
b1=sprintf('0.0015, 3, Composite, %1.4f, L1',New01);
b2=sprintf('0.0015, 3, Composite, %1.4f, L2',New02);
b3=sprintf('0.0015, 3, Composite, %1.4f, L3',New03);
b4=sprintf('0.0015, 3, Composite, %1.4f, L4',New04);

%Use the function "strrep" to replace old string (1e+07, 0.3) with new
%string (2e+07, 0.3)
% Edit below
CurrentFile{1135}=strrep(a5,CurrentFile{1135},b1);
CurrentFile{1136}=strrep(a6,CurrentFile{1136},b2);
CurrentFile{1137}=strrep(a7,CurrentFile{1137},b3);
CurrentFile{1138}=strrep(a8,CurrentFile{1138},b4);

% Edit above
```

```
%Open new input file
TestCount=TestCount+1;
NewINPName=sprintf('Test%g.inp',TestCount);
fid = fopen(NewINPName,'w');
%Write to new file
for l=1:length(CurrentFile)
     fprintf(fid,'%s\n',CurrentFile{l});
end
fclose(fid);
NewINP=NewINPName;
```

Run Abaqus Script and Retrieve Information

```
% Runs a python script that query the history of the displacement and
% reaction force of the beam job and write that history to *.dat* file
% then print the queried data as AbaqusData
function AbaqusData=RunScript()
format longe
!abaqus cae noGUI=ExtractScript.py
U1=importdata('U1.dat');
U2=importdata('U2.dat');
TS=importdata('TS.dat');
AbaqusData=zeros(1,3);
if size(U1)==0
    AbaqusData(1,1)=0;
    AbaqusData(1,2)=0;
else
    for y=1:length(U1(:,1))
        AbaqusData(y,1)=U1(y,2);
        AbaqusData(y,2)=U2(y,2);
        AbaqusData(y,3)=TS(y,2);
    end
end
AbaqusData
```

Abaqus Python Script to Retrieve Data

```
from odbAccess import *
from abaqus import *
from abaqusConstants import *
odb = openOdb(path='ChassisTest.odb')
step2 = odb.steps['Step-1']
region = step2.historyRegions['Node PART-1-1.297']
u1Data = region.historyOutputs['U1'].data
dispFile = open('U1.dat','w')
for time, u1Disp in u1Data:
    dispFile.write('%10.4E   %10.4E\n' % (time, u1Disp))
dispFile.close()
u2Data = region.historyOutputs['U2'].data
dispFile = open('U2.dat','w')
for time, u2Disp in u2Data:
    dispFile.write('%10.4E   %10.4E\n' % (time, u2Disp))
dispFile.close()
TSData=odb.steps['Step-1'].frames[1].fieldOutputs['TSAIW'].values[0].data
dispFile = open('TS.dat','w')
dispFile.write('%10.4E   %10.4E\n' % (time, TSData))
dispFile.close()
```